nature communications

Article

https://doi.org/10.1038/s41467-025-57808-4

Nf2-FAK signaling axis is critical for cranial bone ossification and regeneration

Received: 19 April 2023

Accepted: 5 March 2025

Junguang Liao[1,6], Yuping Huang[1,6], Fuju Sun[1], Chenggong Zheng[1], Yifeng Yao[1], Cui Zhang[2], Chenhe Zhou[3], Xingen Zhang[4] ✉, Mengrui Wu[5] ✉ & Guiqian Chen[1] ✉

Skeletal mesenchymal stem cells (MSCs) possess self-renewal capacities and play a leading role in the craniofacial system. However, their engagement in controlling cranial bone development and regeneration remains largely unidentified. Herein, we discovered the *neurofibromin* 2 (*Nf2*)-encoded regulator Merlin, demonstrating indispensableness in the craniofacial system. Mice lacking *Nf2* in MSCs exhibit malformed cranial bones, diminished proliferation, increased apoptosis, and more severe osteogenesis impairment. Mechanically, we substantiate that Nf2 physically interacts with focal adhesion kinase (FAK) to preferentially mediate Erk1/2 and PI3K catalytic p110 subunit/Akt signaling. Meanwhile, Nf2-FAK disturbance in MSCs results in deficient migration, cytoskeletal organization and focal adhesion dynamics, and develops retarded regeneration of cranial bone defects. Collectively, our findings underscore an unrecognized scaffolding role for Nf2-FAK as upstream element in regulating PI3K/Akt and Erk1/2 action in osteoblasts, and illuminate its essentialness in coordinating cell migration, osteogenic lineage development, cranial bone ossification and regeneration.

The skull is a requisite bone that plays a central role in regulating stable brain development and growth. The morphogenesis of cranial bones is exquisitely organized during the embryonic and postnatal stage. The skeletal mesenchymal stem cells (MSCs) are vital for the development, construction, and remodeling of cranial bones. The commitment and recruitment of MSCs to differentiate into osteoblast lineage is critical for the calvaria formation[1–6]. The disturbance in this process gives rise to serious birth defects or skeletal deformities[7,8]. Moreover, cranial MSCs, harboring in the postnatal sutures, are competent to be invigorated and emigrated towards injury sites to restore bones defects[9–11]. Manipulating MSCs was found sufficiently repairing craniofacial birth defects[12]. Therefore, the concerted migration and differentiation of MSCs exerts a significant influence for osteoblast lineage development, cranial bone formation and the repair of skull defects.

Focal adhesion kinase (FAK) is an intracellular non-receptor tyrosine kinase and has been documented essentially to guide mesenchymal stem cells differentiate to osteoblasts[13–15]. FAK governs osteoblast proliferation, differentiation[16], osteoblast-adipose commitment shift[17], collagen synthesis[18] and bone regeneration[19]. FAK and its mediated signaling were indicated through MAPK[20], PI3K/Akt[21,22] or mTOR[16] in osteoblasts. Moreover, FAK plays essential role in cell migration, and FAK triggers focal adhesion positioning[23], establishes sub-areas within focal adhesions[24] and modulates cell protruding[25]. Focal adhesion (FA) dynamic is a continued process connecting the

---

[1]Department of Biopharmaceutics, Zhejiang Provincial Engineering Research Center of New Technologies and Applications for Targeted Therapy of Major Diseases, College of Life Science and Medicine, Zhejiang Sci-Tech University, Hangzhou 310018, China. [2]Affiliated Hangzhou First People's Hospital, Zhejiang University School of Medicine, Hangzhou, China. [3]Department of Orthopedics, Second Affiliated Hospital, Zhejiang University School of Medicine, Hangzhou, China. [4]Department of Orthopedics, Jiaxing Key Laboratory for Minimally Invasive Surgery in Orthopaedics & Skeletal Regenerative Medicine, Zhejiang Rongjun Hospital, Jiaxing 314001, China. [5]Department of Cell and Developmental Biology, College of Life Sciences, Zhejiang University, Hangzhou, China. [6]These authors contributed equally: Junguang Liao, Yuping Huang. ✉e-mail: zhxg66@126.com; mengruiwu@zju.edu.cn; gqchen@zstu.edu.cn

adjustment between FA and actin cytoskeleton[26,27]. FAK accumulates at the emerging FAs earlier at cell front[27]. However, it is still largely unknown how FAK activity is determined to direct MSC migration and osteoblast differentiation.

Neurofibromin 2 (Nf2) encodes a protein called Merlin and firstly named in patients with Neurofibromatosis Type 2 disease[28–30]. Merlin is a 70-kDa member of the Ezrin-Radixin-Moesin branch of the band 4.1 protein superfamily. Merlin consists of an N-terminal FERM domain, a central α-helical region, and a C-terminal domain (CTD). The intermolecular FERM-CTD interaction change allows Merlin to transit into an open (proliferation-permissiveness) or a closed (proliferation-inhibition) transformation. *Nf2*/Merlin was widely known as a tumor suppressor, but mechanism varied in various tumor cells[31–33]. Remarkably, *Nf2* extensively expressed at E6.5 and in migrating neural crest cells at E8.5[34], which was a critical cell lineage for skull development[3,4]. *Nf2* was found expressed in frontal and parietal bone[35]. *Nf2* mutant mice failed to launch the gastrulation[36]. *Nf2* in hematopoietic stem cells maintains the homeostasis of hematopoietic stem cell niche and confine bone and vascular components[37]. However, how *Nf2* performs in bone cells is still principally undetermined.

To characterize molecular function of *Nf2*/merlin in cranial bones, we generate a skeletal tissue-specific knockout mice model of *Nf2* using *Prx1-Cre*, a generally used transgenic mouse line to label skeletal mesenchymal stem cell[38,39], and inducible *Prx1-CreER*, which exclusively mark suture stem cells that important for bone regeneration of cranial defects[40,41]. Our data demonstrate that *Nf2* acts as an upstream regulator to mediate FAK activity and Nf2-FAK reciprocity is indispensable in regulating MSC migration, osteoblast lineage differentiation, cranial bone formation and regeneration.

Results

Nf2 knockout in skeletal mesenchymal cells impaired the morphogenesis of cranial bones

In our study, *Nf2* gene product, Merlin, was found expressed in brain, liver, spinal cord, skull and limb tissues at 18.5 embryonic stage (Fig. 1a, upper panel). In skull tissues, Merlin also maintained higher expressions at early postnatal cranial tissues (Fig. 1a, lower panel). To characterize the function of *Nf2* in bone tissues, *Nf2* floxed allele (*f/f*) mice from Inserm[42] was introduced and its conditional knockout was generated using *Prx1-Cre*, which essentially mark skeletal mesenchymal cells[38,43], including frontal and parietal bone but not dura mater[44]. *Nf2* knockout mice (*Nf2-cKO*) mice presented severe skeletal deficiencies, such as smaller body size and irregular cranial bones (Fig. 1b–d). This phenotype was uniform to skeletal deformities observed using inducible *Prx1-CreER* mediated *Nf2* deletion (Supplemental Fig. S1a–c), and *Nf2* mutant mice died post-delivery, probably from asphyxia due to non-fusion sternum during the development (Fig. S1d, red arrow).

At the craniofacial level, *Nf2-cKO* mice displayed deformed appearance, the angles from the body axis to the head were significantly enlarged compared to littermate controls (E15.5 $p < 0.0001$; P1 $p < 0.0001$, $n = 3$) (Fig. 1b, Fig. S1e). Using skeletal staining (E16.5-P1) and *micro-CT* (P1, Fig. S1f) to visualize the skeletal integrity, we found that *Nf2-cKO* mice exhibited unossified empty frontal and parietal bone, and partially the intraparietal bones (Fig. 1c, d, red arrow). At coronal level, the width distance between two parietal bones (Fig. 1c, red arrow) was significantly expanded in *Nf2-cKO* compared to the litter controls (Fig. S1g, E16.5 $p < 0.0001$; E18.5 $p < 0.0001$; P1 $p < 0.0001$, $n = 3$). The distances between nasal bone and coronal suture (Fig. 1c, black arrow) were a significantly elongated in *Nf2-cKO* compared to the controls (Fig. S1h, E16.5 $p < 0.0001$; E18.5 $p < 0.0001$; P1 $p = 0.011$, $n = 3$) (Fig. 1g), suggesting a malformed skull size in *Nf2* mutant mice.

Due to the severe affected frontal bone and parietal bone in *Nf2-cKO* mice, we scanned E18.5 *Nf2-cKO* and littermate control mice using micro-CT and reconstructed the 3D images[45] (Fig. 1d–e, $n = 8$). We found that the volume of defective frontal and parietal bone (Fig. 1f1, $p = 0.0005$; Fig. 1g1, $p = 0.0072$), the ratio of the defective volume relative to its respective bone volume (Fig. 1f2, $p < 0.0001$; Fig. 1g2, $p = 0.0384$) were both significantly diminished in *Nf2-cKO* mice. The ratio of surface defect area relative to the whole frontal bone (Fig. 1f3, $p < 0.0001$) and parietal bone (Fig. 1g3, $p < 0.0001$) were significantly increased in *Nf2* mutant mice. Next, we isolated frontal bone (Fig. 1h, $n = 8$) and parietal bone (Fig. 1j, $n = 8$) from E18.5 control and *Nf2-cKO* mice and located the anatomical landmarks (Fig. 1h1, j1, triangle indicated) and compared the size especially. In frontal bones, *Nf2* mutant mice displayed significant reduction on lateral bone size between points 2–3 (Fig. 1i1, $p = 0.00054$) and points 1–3 (Fig. 1i1, $p = 0.0025$) but not significant difference in points 1-2 (Fig. 1i1, $p = 0.467$), significant increase on defect width between points 1–1 (Fig. 1i2, $p < 0.0001$), 2–2 (Fig. 1i2, $p = 0.001$) and 3–3 (Fig. 1i2, $p = 0.0002$), and the ratios of width defect ratio relative to points 3-3 (1-1/3-3, 2-2/3-3) were significantly increased (Fig. 1i3, $p < 0.0001$). In parietal bones, we found that length distances between points 1–2 (Fig. 1k1, $p < 0.0001$), 3–4 (Fig. 1k1, $p < 0.0001$), 1–3 (Fig. 1k1, $p = 0.012$), and 2–4 (Fig. 1k1, $p = 0.001$) were significantly reduced, the width defect distances between points 1-1 (Fig. 1k2, $p = 0.007$), 2–2 (Fig. 1k2, $p = 0.0005$), 3-3 (Fig. 1k2, $p = 0.001$) and 4–4 (Fig. 1k2, $p < 0.0001$) were significantly disorganized, the ratios on 1-1/2-2 (Fig. 1k3, $p = 0.0012$) and 3-3/4-4 (Fig. 1k3, $p < 0.0001$) were significantly increased in *Nf2* mutant mice, thus presenting severely affected bone volume, surface area, size and shape in frontal and parietal bones in *Nf2* mutant mice. Collectively, these data have demonstrated that *Nf2* in skeletal mesenchymal cells plays a leading role in shaping the morphogenesis of cranial bones during the development.

Nf2 deficiency in MSCs resulted in a disrupted osteogenic lineage development

Cranial primordium is initially structured to advance cranial bones formation. Firstly, we showed that *Nf2* expression in Runx2$^+$ labeling osteoprogenitor was effectively reduced at the section of cranial primordium of *Nf2* mutants at E12.5 (Fig S2a). Next, coronal cranial primordium sections at E12.5 were co-stained with Runx2 and EdU (Fig. 2a) to evaluate the cell proliferation. In *Nf2-cKO* mutants, the number of Runx2$^+$ labeling osteoprogenitors was significantly reduced compared to the control (Fig. 2b, $p = 0.026$, $n = 3$), and EdU$^+$/Runx2$^+$ ratio was declined with a mild significance in *Nf2-cKO* mutants compared to the control (Fig. 2c, $p = 0.034$, $n = 3$), and EdU$^+$/Runx2$^-$ ratio was not altered in *Nf2-cKO* mutants compared to the control (Fig. 2d, $p = 0.616$, $n = 3$), suggesting that *Nf2* deletion in skeletal MSCs leads to attenuated proliferation in EdU$^+$ osteoprogenitors. Besides, TUNEL$^+$ immunosignals in *Nf2-cKO* were found increased in Runx2$^+$ osteoprogenitors (Fig S2b, arrow, $p < 0.0001$, $n = 6$), suggesting that apoptosis was increased in Runx2$^+$ osteoprogenitors. Alkaline Phosphatase (ALP) staining was used to evaluate the activities of pre-osteoblasts and osteoblasts at histological level, we found that *Nf2* mutant mice exhibited remarkably reduced activities of osteoprogenitors at E12.5, and the extents and distributions of osteoprogenitors, pre-osteoblasts and mature osteoblasts were dramatically deficient from E12.5 to E17.5 (Fig. 2e, f, arrow). von Kossa staining was used to evaluate ossification process, and we found that *Nf2* mutant calvaria was minimally ossified for most cranial regions at E18.5 sagittal section of cranial bone (Fig. 2g, arrow). Consequently, the immunosignals of osteoblasts-special markers osteopontin (OPN)$^+$ (Fig. 2h, arrow), Runx2$^+$(Fig. 2i, arrow), and Osterix/Sp7$^+$ (Fig. 2j, arrow) were hardly detected at E18.5 sagittal section of cranial bone in *Nf2* mutant mice, suggesting that osteogenic differentiation was more severely impaired in *Nf2* mutants.

Using calvaria primary osteoblast culture system, the same number of osteoblasts were seeded and induced for osteoblast differentiation at D7 and D14. ALP (D7) (Fig. 2k) and Alizarin S Red staining (D14) (Fig. 2l) showed that osteoblast differentiation and ossification was seriously reduced in *Nf2* mutants. *Nf2* mutant osteoblasts were found easy to detach from the plate. In primary pre-osteoblasts, the level of PCNA (proliferating cell nuclear antigen) in *Nf2* mutants was significantly reduced (Fig. 2m, S3a, $p = 0.0166$, $n = 3$), and the levels of *cyclin D1* and *PCNA* were significantly declined (Fig. 2o, $p < 0.0001$, $n = 3$). The osteoblast marker genes (*ALP*, *Runx2*, *Sp7*, *Osteocalcin* (*OCN*), *Type I collagen* (*Col1*), *Fibronectin* (*FN*), *Bone sialoprotein (BSP)*) were significantly decreased at D7 (Fig S3b, $n = 3$) and D14 (Fig. 2p, $n = 3$). The expressions of osteoblastic transcriptional factors (Runx2, Osterix/Sp7) and the secretion of type I collagen by mature osteoblasts (Fig. 2n, $n = 3$) were substantially diminished (Fig S3a, $n = 3$). Besides, *Dlx5* was an essential transcription factor for the differentiation of calvarial osteoblasts. *Dlx5* mutant mice was shown delayed skull ossification[46]. *Msx1/2* double knockout mice displayed rigorous defects in skull formation[47], and the quantity and proliferation of

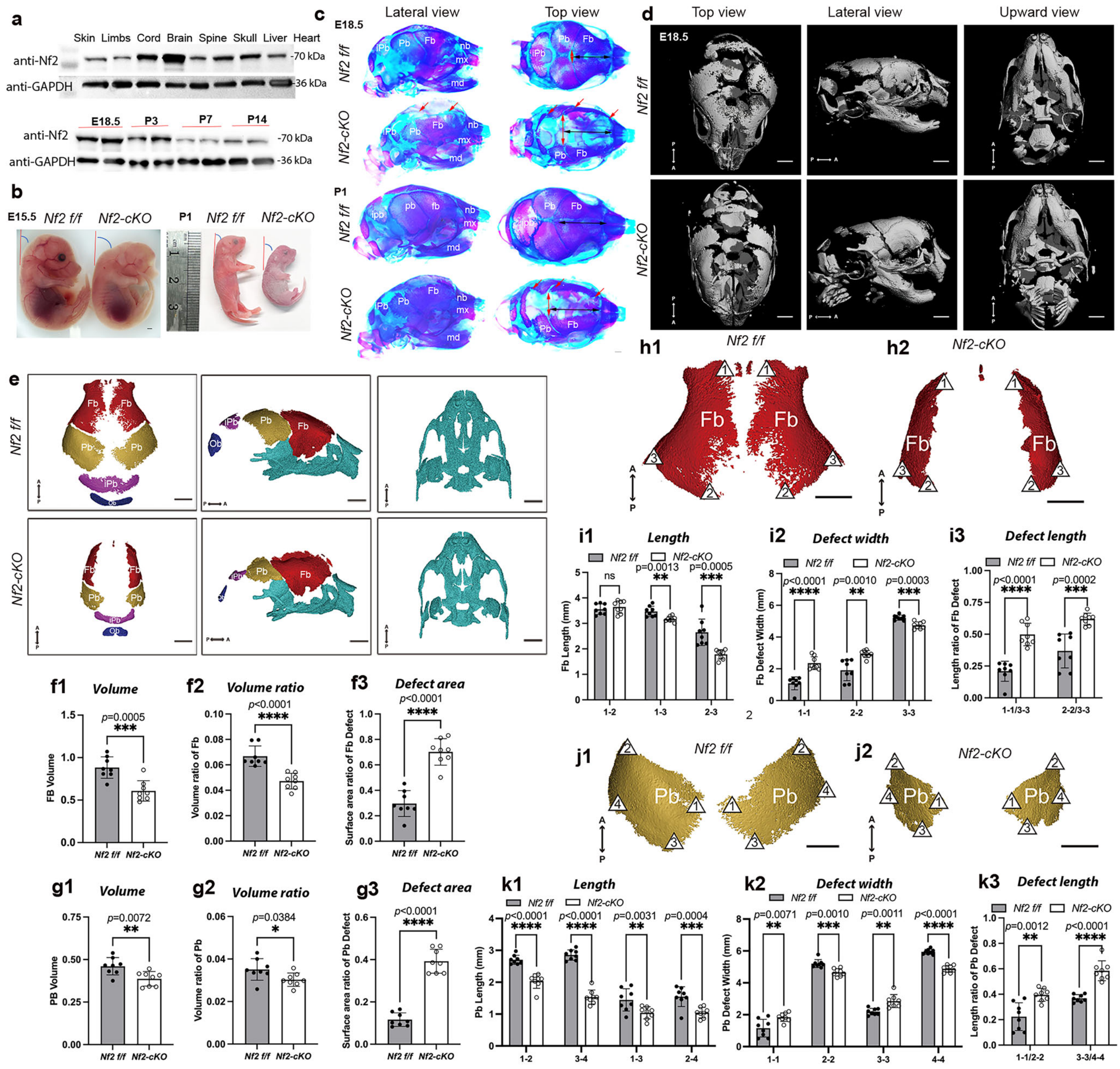

Fig. 1 | *Nf2* knockout in skeletal MSC impaired cranial bones development. a *Nf2* gene coding protein merlin was expressed in various tissues at embryonic 18.5 stage (upper panel, $n = 3$), as well as the embryonic 18.5 and postnatal (P3, P7, P14) skull tissues (lower panel, $n = 3$). **b** *Nf2-cKO* using *Prx1-Cre* resulted in severe birth defects in head shape and limbs, and skeletal staining (**c**) and micro-CT (**d**) showed *Nf2-cKO* led to serious deformities in frontal and parietal bones. The distance between two frontal bones (**c**, red arrow) were significantly wide, and the distances (**c**, black arrow) between nasal bone and coronal suture were notably enlarged in *Nf2* mutant compared to the control ($n = 3$) at E18.5 and P1. **e** 3D reconstruction from micro-CT images of cranial bones from E18.5 control ($n = 8$) and *Nf2-cKO* ($n = 8$). Isolated frontal bone (**h**) and parietal bone (**j**) from E18.5 control and *Nf2-cKO* mice. **i**, **k** Quantification of the size (length and width) of frontal bone (**i1**–**3**) and parietal bone (**k1**–**3**) of E18.5 control and *Nf2-cKO* ($n = 8$). **f**, **g** Quantification of the volume, volume ratio, and surface defect area ratio of the frontal (**f1**–**3**) and parietal bone (**g1**–**3**) from E18.5 controls and *Nf2-cKO* ($n = 8$). Scale bar=50 µm in (**b**, **c**) and 1 mm in (**d**, **e**, **h**, **j**). Data were expressed as means ± SD and each dot represents an individual biological replicate. *P* values were calculated by unpaired Student's t-test with two-tailed analysis without adjustments. $^{***}p < 0.001$, $^{**}p < 0.01$, $^{*}p < 0.05$. P-A: Posterior to Anterior. *Definition of landmarks in frontal bone*: 1 most anterior-superior point of the frontal bone; 2. most posterior-superior point of the frontal bone; 3. most posterior-lateral intersection of the frontal bone and parietal bone. *Definition of landmarks in parietal bone*: 1. most anterior-superior point of the frontal bone; 2. Most anterior-lateral point of the parietal bone; 3. most posterior-superior point of the frontal bone; 4. most posterior-lateral intersection of the parietal bone and interparietal bone. Abbreviation: Fb, frontal bone; Pb, parietal bone; iPb, interparietal bone; nb, nasal bone; mx, maxilla; md, mandible. Ob, occipital bone.

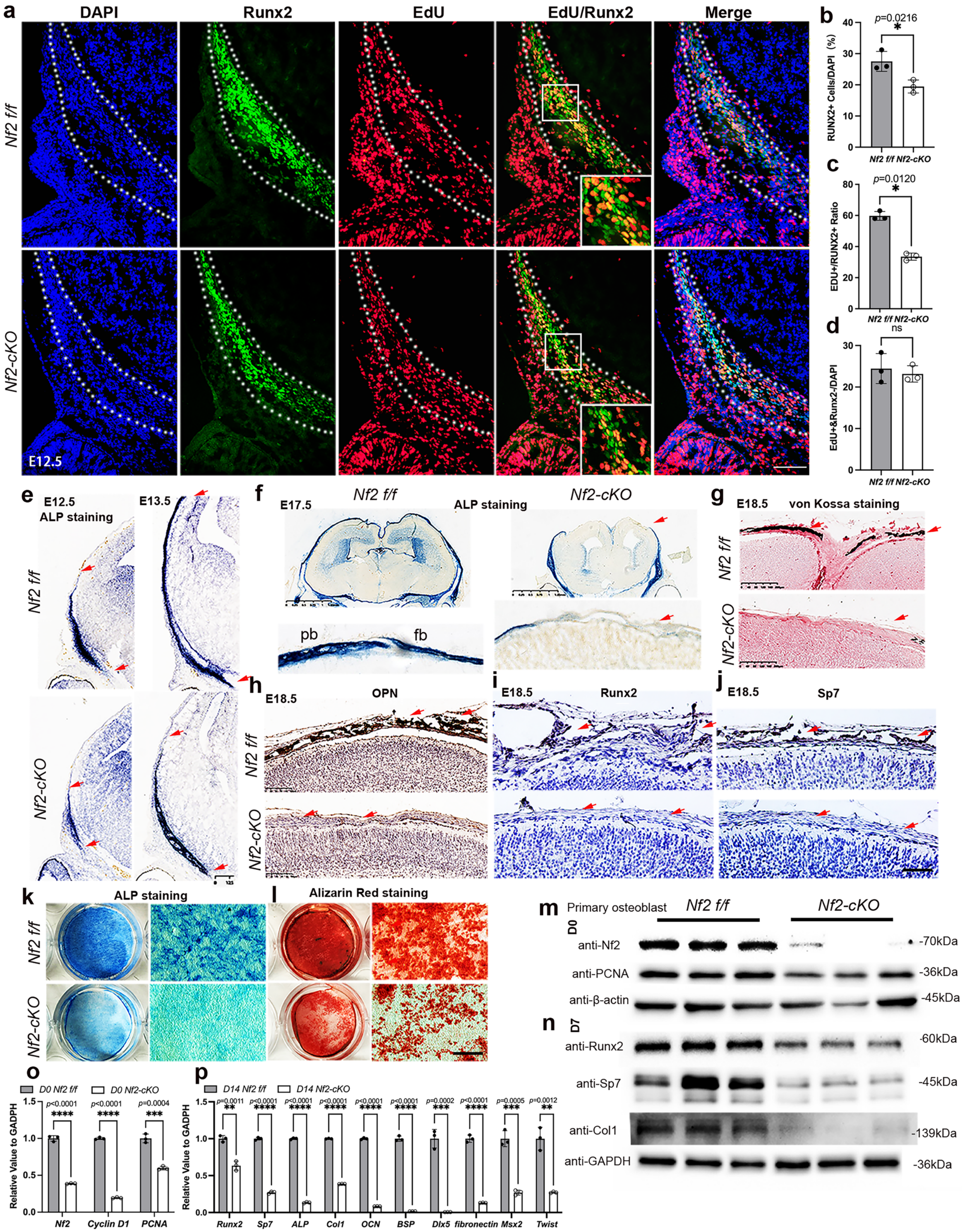

skeletogenic mesenchyme were decreased in *Msx2-Twist* double mutants[48]. We found that *Dlx5, Msx2, Twist1/2* were dramatically declined in *Nf2* mutant osteoblasts at D7 (Fig S3b, $n = 3$) and D14 stage (Fig. 2p, $n = 3$). These data unveiled that *Nf2* in mesenchymal stem cell in vivo is indispensable to orchestrate a standard osteogenic lineage development.

Nf2 was required for cell migration, adhesion, and cytoskeletal organization

Due to the defects that massive unossified cranial tissues and loosen primary osteoblasts in *Nf2* mutants, we wondered whether it was due to the flaws in pre-osteoblasts migration and adhesion. We performed a scratch-wound assay to evaluate cell migrations and found decreased

Fig. 2 | *Nf2* deficiency in skeletal MSC disrupted osteoblast lineage development. a Immunofluorescence images of EdU and Runx2 co-labeled osteoprogenitors at E12.5 coronal section of skull tissues. The percentage of Runx2$^+$ cells (**b**), EdU$^+$/Runx2$^+$ ratio (**c**), EdU$^+$/Runx2$^-$ cells (**d**) were analyzed in the E12.5 controls and *Nf2* mutants. **e**, **f** *Nf2-cKO* showed noticeably reduced extent of osteoblast activities and ossification using ALP staining at E12.5 and E17.5. **g** von Kossa staining showed remarkably reduced ossification in *Nf2* mutants at the sections of E18.5 sagittal calvaria. Immunosignals of OPN (**h**), Runx2 (**i**) and Sp7 (**j**) were hardly found in *Nf2* mutant sagittal calvaria at E18.5. In calvaria primary osteoblast culture system, ALP staining (**k**) and Alizarin S Red staining (**l**) showed severely impaired osteoblast differentiation and mineral matrix formation at D7 and D14, respectively. PCNA were significantly decreased at protein and gene expression levels in *Nf2* mutant preosteoblasts (**m**, **o**). The activities of Runx2, Sp7 and collagen type (**l**) were significantly decreased in *Nf2* mutant osteoblasts at D7 (**n**). *Nf2-cKO* osteoblast showed significantly declined levels of marker genes expressions (*ALP, Runx2, Sp7, OCN, Col1, fibronectin, BSP, Dlx5, Msx2, Twist1/2*) at D14 (**p**). Scale bar=50 μm in (**a**, **h**–**m**). scale bar=20 μm in (**e**–**j**). Data were expressed as means ± SD and each dot represents an individual biological replicate. *P* values were calculated by unpaired Student's t-test with two-tailed analysis without adjustments. *$p < 0.05$. **$p < 0.01$, ***$p < 0.001$. abbreviation: Proliferating cell nuclear antigen (PCNA), Alkaline phosphatase (ALP), Osteopontin (OPN), Osteocalcin (OCN), bone sialoprotein (BSP), Type I collagen (Col1).

migration but with no notable difference in osteoblast migration in *Nf2* mutants compared to the control (Fig. S4a, b, dotted red line). Then, we tested if cranial MSCs migration was deficient, to lessen the consequence of proliferation in *Nf2* mutants, the collected primary suture MSCs[49,50] were firstly used to be transfected with lentivirus mediated knockdown of *Nf2* in culture medium with no FBS supplement, and the healing distances at different time interval after the scratch-wound were calculated and analyzed, and we found that the healing distance was significantly reduced in *Nf2* knockdown MSC compared to that in the controls at 12 h ($p = 0.032$, $n = 3$) and 24 h ($p = 0.017$, $n = 3$) (Fig. S4c, d). Meanwhile, the same migration assay was performed using *Nf2* control and *Nf2-cKO* MSC (Fig. 3a, dotted line), and we observed that the healing distance was significantly declined in *Nf2-cKO* MSC compared to that in the controls at 12 h ($p = 0.016$, $n = 8$), 24 h ($p < 0.001$, $n = 8$), 36 h ($p < 0.001$, $n = 8$) and 48 h ($p < 0.001$, $n = 8$) (Fig. 3a, b).

Next, cell adhesion and detachment in osteoblasts were evaluated. After plating the same number of primary osteoblasts for different times, the non-attached cells were washed off with caution, the remnant osteoblasts were stained with crystal violet solution and counted. We found that *Nf2* mutant osteoblasts showed significantly lower capacity for the cell adhesion at post-plating 30 min (Fig. 3c, $p < 0.001$, $n = 3$). Similarly, the detachment assay was performed, and 80–90% confluent primary osteoblasts were incubated using 0.2% EDTA for 10 min, and the remnant adherent osteoblasts were numbered. We found that the number of adherent osteoblasts after 0.2% EDTA treatment in *Nf2* mutants was notably diminished compared to the control (Fig. 3d, $p = 0.0045$, $n = 3$), suggesting that adherent *Nf2* mutant osteoblasts were easier to be detached compared to the controls. Cytoskeletal arrangement was requisite for cell migration, F-actin and β-Tubulin were primary cytoskeleton proteins, and the immunosignals showed a chaotic cytoskeletal assembly in *Nf2* mutant osteoblasts (Fig. 3e). GTPase activity was one influential adjustor in cytoskeleton, and we found that the activity of RhoA enzyme was specially decreased in *Nf2* mutant MSCs using rhotekin-RBD beads pulling down the RhoA in lysate (Fig. 3f, $p = 0.0010$, $n = 3$). These data illuminated that *Nf2* is principally required for normal cell migration, adhesion and cytoskeleton organization in MSCs and osteoblasts.

Nf2 deficiency led to defective focal adhesion formation

To explore the potential cause of defective migration and adhesion in *Nf2* mutants, we tested how focal adhesion was altered. Focal adhesion (FA) dynamics were a constant manner engaging in adjusting between FA and actin cytoskeleton[26,27]. The spatial-temporal localization of Paxillin played essential roles in FA formation and is necessary for FA turnover during cell migration[51,52]. Paxillin mutations affected focal adhesions[53]. We found that phospho-Paxillin-labeled focal adhesion was extensively distributed in protrusion of cell fronts in control after plating cells at 3 h, and the phospho-Paxillin-labeled focal adhesion was attached to numerous actin stress fibers in FA (Fig. 4a, b), but *Nf2* mutant MSC showed markedly reduced formation of focal adhesion (Fig. 4b, arrow) and actin stress fibers in the mutant cells (Fig. 4a, b). The area of FA size (Fig. 4b, arrow) was significantly declined in *Nf2* mutants (Fig. 4c, $n = 12$, $p = 0.0387$). Due to the difficulty to transfect the *Paxillin-GFP* plasmid into MSC, we then transfected *Paxillin-GFP* plasmid directly into primary osteoblasts. After 24 h, the primary osteoblasts were digested and plated in fibronectin-precoated plates for live cell imaging to estimate the proceeding of cell adhesion. We found that the distributions of *Paxillin-GFP* labeled FA were properly grown and diffused at the fronts in primary osteoblasts of the control (Fig. 4d, d' arrow). However, in *Nf2* mutant osteoblasts, we found that *Paxillin-GFP* labeled FAs were mostly situated in cytoplasm and less at the fronts (Fig. 4d, d" arrow). The ratio between the cells with properly formed *Paxillin-GFP*-labeled FA at the fronts and total cells showed a notable decrease in *Nf2* mutants compared to the controls ($p < 0.001$, $n = 3$) (Fig. 4e), suggesting that the focal adhesion formation at the fronts was considerably inactive in *Nf2* mutant osteoblasts, which may be the cause for the phenotype that *Nf2* mutant osteoblasts disclosed deficient adhesion and delayed migration. These data presented that *Nf2* is essentially important for the formation of focal adhesion dynamics in part through the regulation of Paxillin.

Nf2 acted as an upstream regulator to mediate FAK activity with a physical interaction

Mechanically, we found that the level of phospho-397 FAK, a momentous site for cellular FAK action, was declined in *Nf2* mutants (Fig. 5a), implying that FAK may function as a downstream factor of Nf2. At sections of cranial primordium at E12.5, we demonstrated that the immunosignals of p-FAK (397) were predominantly reduced in Runx2$^+$ osteoprogenitor in *Nf2* mutant mice (Fig. 5h, arrow). At late stage of cranial bone development at E18.5, we confirmed that immunosignals of p-FAK (397) were substantially diminished in *Nf2* mutants (Fig. 5i, arrow) on sagittal sections of the skull. While the overexpression of *Nf2* or *FAK* in *Nf2* mutant osteoblasts was effectively rescued deficient phenotype of *Nf2* mutant osteoblasts for 5 days using ALP staining (Fig. 5b). Additionally, overexpression of *Nf2* in *Nf2* knockout osteoblasts can sufficiently rescue the levels of phospho-397FAK, collagen type 1, Runx2 and SP7 in *Nf2* mutant osteoblasts (Fig. 5c), thus presenting that Nf2 works as an upstream regulator to modify FAK activity in osteoblasts.

In osteoblasts, how FAK is regulated is unidentified. To evaluate the interactive role between Nf2 and FAK in osteoblasts, we generated the transient plasmids for FAK and Nf2 with a tag protein FLAG and HA using the HEK293T cell. In vitro co-immunoprecipitation assay (co-IP) showed that FLAG-FAK and HA-Nf2 formed a complex (Fig. 5d), and single transfection of either FLAG-FAK or HA-Nf2 as a control (Fig S5). In primary cultured osteoblasts, we certified that FAK interacts with Nf2 protein (Fig. 5e). Thereafter, we applied the NanoBiT protein, a protein interaction system, which has been demonstrated to be an effective tool in discerning protein interaction in live cells based on structural complementation[54,55]. We made all the plasmids for FAK and Nf2 fuse proteins blended with large BiT and small BiT domains based on individual amino acid directions (N2015, Promega) (Fig. 5f). Then the plasmids containing with large or small BiT domains were transfected into osteoblast cell line MC3T3-E1 (3T3) to examine the

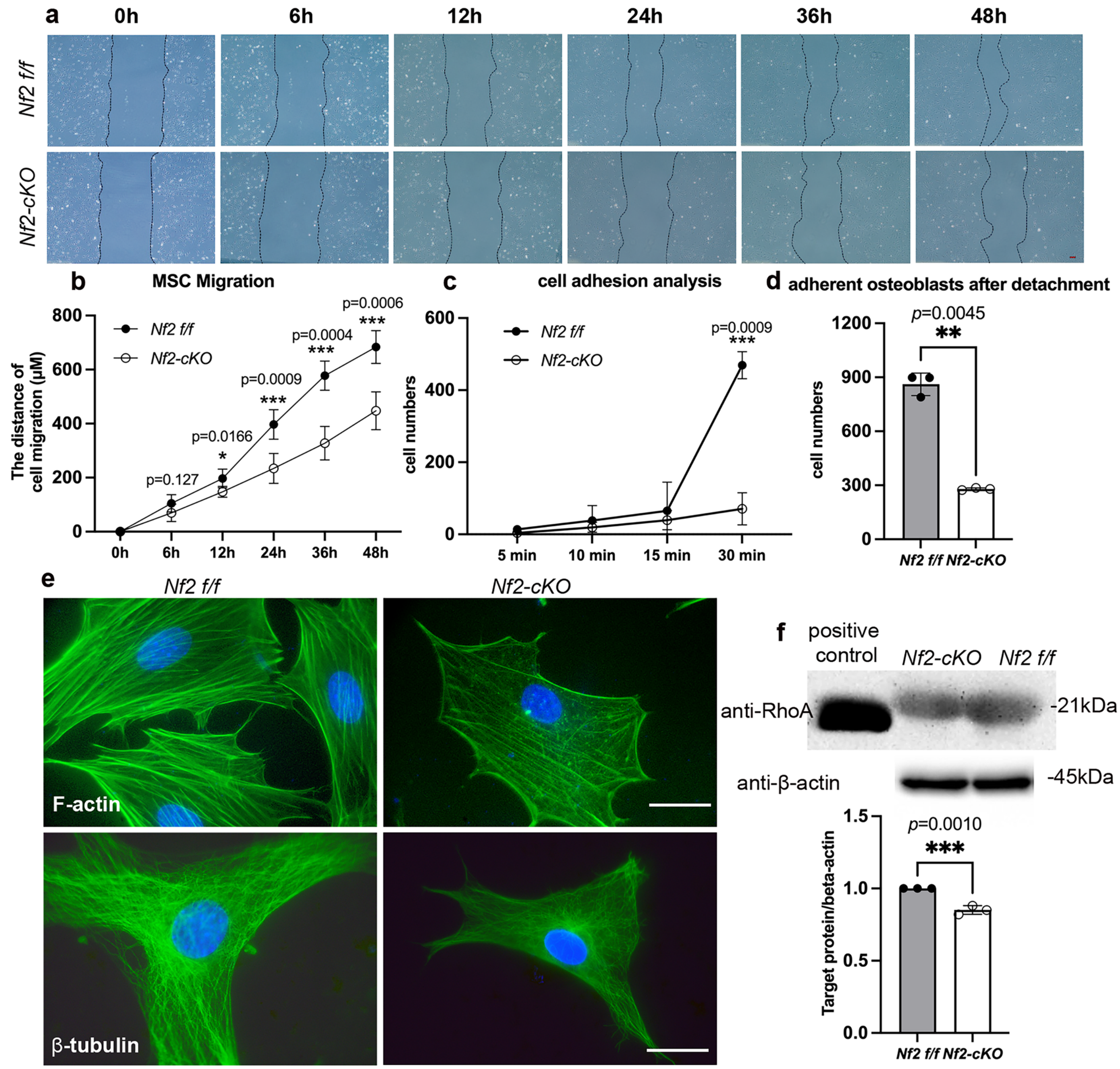

Fig. 3 | *Nf2* deletion resulted in defective cell migration, adhesion, and attachment. a A scratch-wound assay was performed to examine MSC migration that isolated from *Nf2* control and *Nf2* mutant mice. The healing distances were calculated at each time point and analyzed ($n = 8$) (**b**). **c** Primary osteoblasts were plating on fibronectin precoated plates with no fetal bovine serum for different time points, and the non-attached cells were washed, and the remaining osteoblasts were stained by crystal violet and counted for analysis, and *Nf2* knockout led to significantly diminished cell adhesion. **d** The cultured adherent *Nf2* mutant osteoblasts was significantly reduced after cell detachment experiment using 0.2% EDTA for 10 min. **e** F-actin staining by Phalloidin and β-tubulin staining showed that cytoskeletal assembly was disorganized in *Nf2* mutant osteoblasts. **f** Rhotekin-RBD beads were added to lysate to pull down the RhoA, and Western Blotting were performed to measure the activity of RhoA in *Nf2* mutants (BK030, Cytoskeleton, Inc.) and the data showed that RhoA activity was significantly decreased in *Nf2* mutant MSC. Scale bar= 50 µm in (**a**, **e**). Data were expressed as means ± SD and each dot represents an individual biological replicate. *P* values were calculated by unpaired Student's t-test with two-tailed analysis without adjustments. $^{*}p < 0.05$. $^{**}p < 0.01$, $^{***}p < 0.001$.

bioluminescence that produced based on structural complementation. Our results showed that C-terminal-Nf2 domain in small subunit structurally and physically interacts with N-terminal-FAK domain in large subunit, as a result, a physical Nf2-FAK reciprocity can develop the bioluminescence. The bioluminescence ratio between Nf2-FAK interaction and negative control was about 37.6-fold, which was noticeably greater than the definition of active protein: protein interaction threshold (about 10 folds) ($p = 0.0001$, $n = 3$) (Fig. 5g). Our data demonstrated that Nf2-FAK interaction is physical in structural domain in osteoblasts.

Nf2-FAK interaction preferably mediated PI3K/Akt and Erk1/2 signaling in osteoblasts

FAK mediated signaling is an established intracellular signaling pathway that organizes cell behavior[15]. FAK promoted phospholipase C-gamma activity[56], FAK also functioned as the upstream of PI3K/Akt in fibroblasts[57]. In skeletal cells, FAK was shown mediated intracellular signaling through either MAPK[20], PI3K/Akt[21,22] or mTOR[16]. How Nf2-FAK mediates downstream signaling in osteoblasts is unclear. Our data demonstrated that the activity of phospho-PLC-γ decreased in *Nf2* mutant osteoblasts (Fig. 6a). Akt was regarded as the principal output

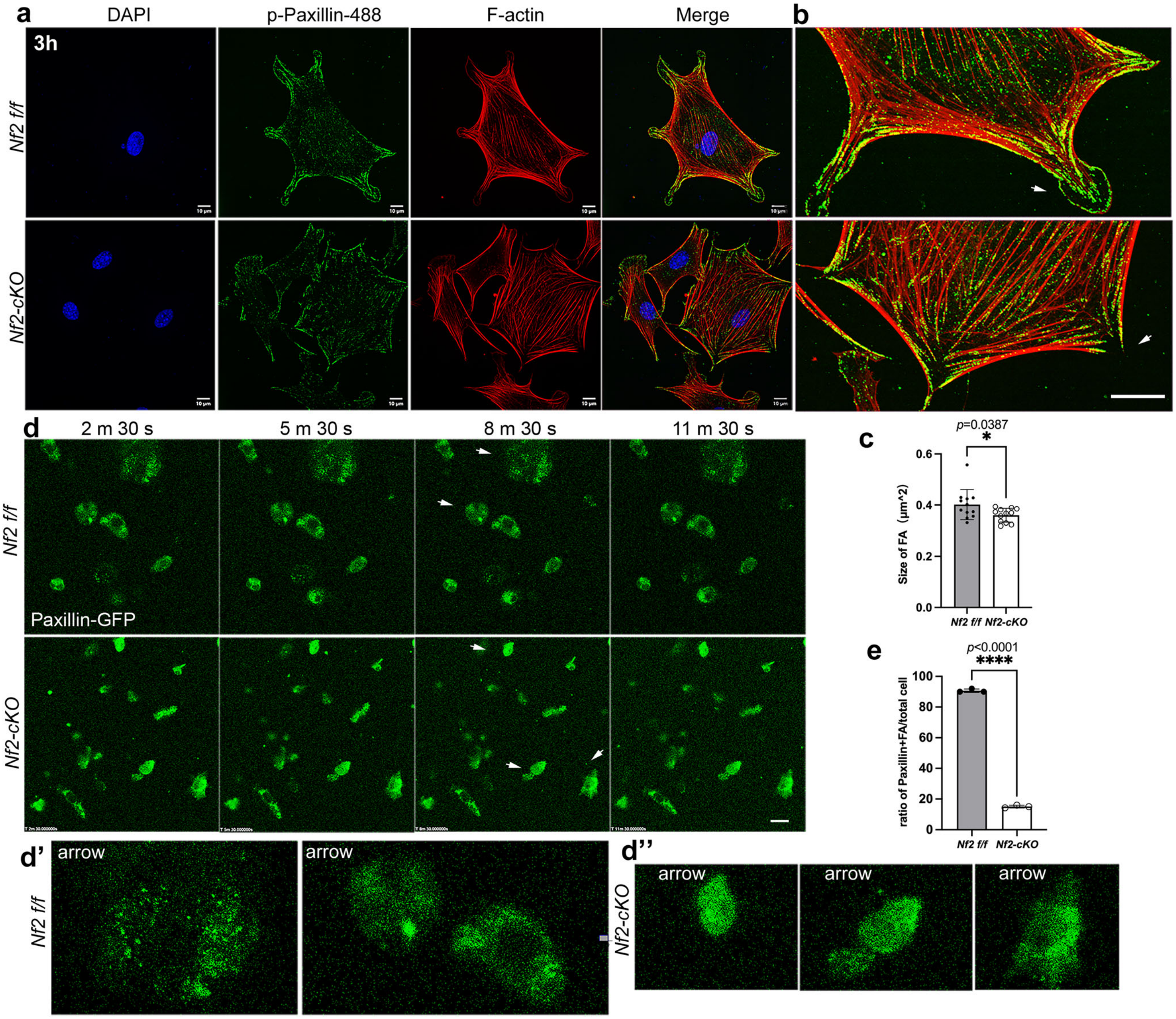

Fig. 4 | *Nf2* disturbance led to deformed focal adhesion dynamics. **a** Confocal images of immunostaining assay showed that the extent of p-Paxillin-labeled focal adhesion and Phalloidin-labeled F-actin in *Nf2* mutant MSC and control. **b** arrow indicated higher magnification of FA in (**a**). **c** The area of FA size was quantified using ImageJ ($n = 12$). **d** Live cell imaging analysis from transient transfection of *Paxillin-GFP* into primary osteoblasts showed that *Paxillin-GFP*-labeled focal adhesion dynamics were properly growing in control osteoblasts (enlarged magnification shown in **d'** in arrow), but *Paxillin-GFP*-labeled focal adhesions were mainly situated in cytoplasm in *Nf2* mutant osteoblasts (enlarged magnification shown in **d''** in arrow). **e** The ratio between properly developed *Paxillin*$^+$ cells and total cells in *Nf2* mutants was notably lower compared to the controls ($n = 3$). Scale bar: 10 μm in (**a**–**c**), 50 μm in (**d**). Data were expressed as means ± SD and each dot represents an individual biological replicate. *P* values were calculated by unpaired Student's t-test with two-tailed analysis without adjustments. $^*p < 0.05$. $^{**}p < 0.01$, $^{***}p < 0.001$.

of PI3K signaling[57], our data confirmed that the activity of phospho-Akt significantly reduced (Fig S3) in *Nf2* mutant osteoblasts, suggesting that PI3K/Akt signaling is altered in *Nf2* mutant osteoblasts (Fig. 6a). Additionally, MAPK signaling pathways, including Erk1/2[58], p38 MAPK[8], and JNK pathways[59], are important signaling for the osteoblast differentiation. Our data exhibited that the activities of phoshpo-p38 and phospho-JNK were not altered in *Nf2* mutants, but the level of phospho-Erk1/2 was significantly declined (Fig. S3a) (Fig. 6b), suggesting that Erk1/2 signaling was particularly disturbed in *Nf2* knockout osteoblasts. At the section of skull tissue at E18.5, the immunosignals of phospho-AKT (Fig. 6f, arrow) and phospho-Erk1/2 (Fig. 6g, arrow) in *Nf2* mutant mice were significantly diminished. At the section of cranial primordium at E12.5, we also authenticated that the immunosignals of phospho-Akt (Fig. 6h, arrow) and phospho-Erk1/2 (Fig. 6i, arrow) were significantly declined in Runx2$^+$ osteoprogenitors in *Nf2* mutant mice compared to the controls. These data exhibited that Nf2-FAK interaction preferentially mediated PI3K/Akt and Erk1/2 signaling in osteoblasts at cellular and histological level.

PI3K is a heterodimer including a p85 regulatory subunit and a p110 catalytic subunit[60], and plays an essential function in osteoblasts differentiation[61,62]. In fibroblasts, FAK was reported to bind PI3K-p85 regulatory subunit to regulate cell behavior[63]. In osteoblasts, how FAK and PI3K/Akt is associated remains unknown. We performed co-IP assay to assess their association in primary osteoblasts, our data revealed that FAK interacts with the catalytic subunit p110 of PI3K complex, and *Nf2* mutant osteoblasts attenuated the connection between FAK and subunit p110/PI3K (Fig. 6c–e), suggesting a direct cellular interplay of Nf2/FAK/p110-PI3K/Akt in osteoblasts. These results uncover a new frame for Nf2-FAK as upstream component in regulating PI3K action in osteoblasts.

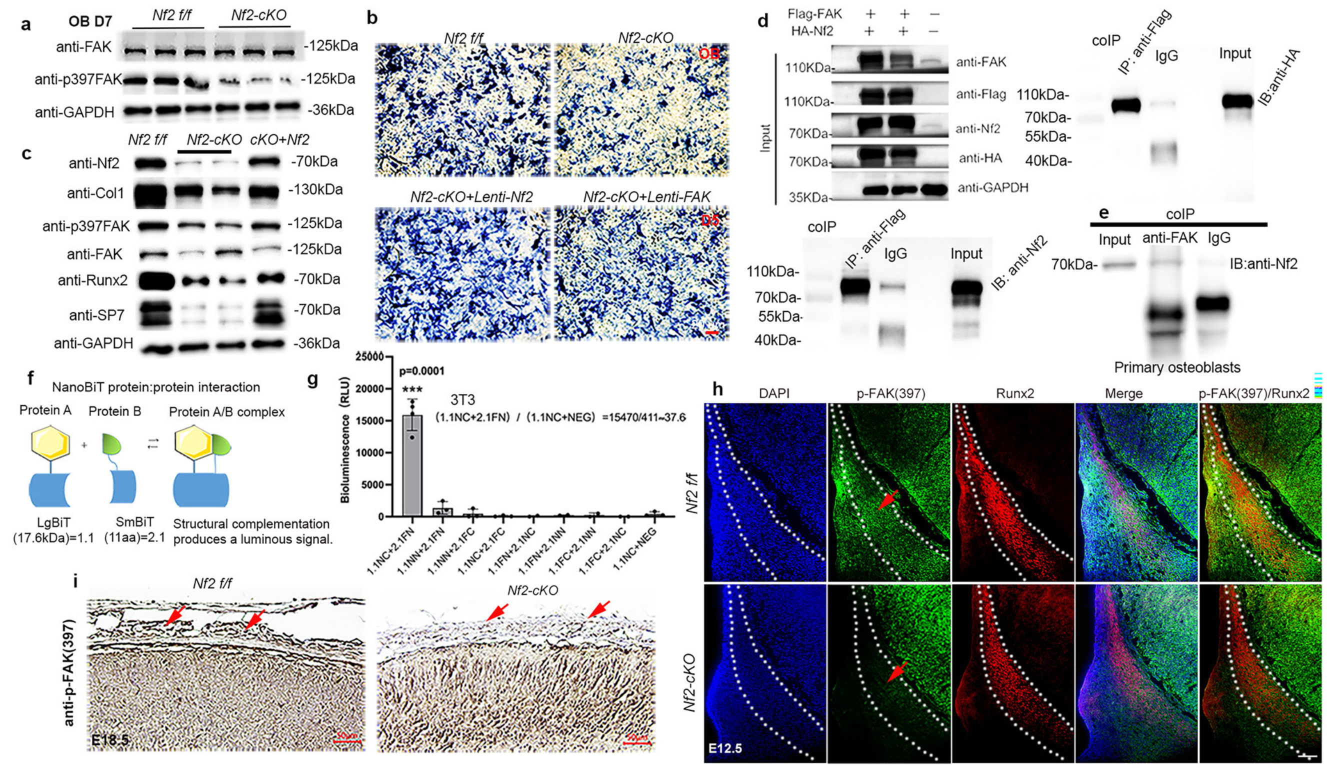

Fig. 5 | *Nf2*-FAK interaction alteration impaired osteoblast differentiation. **a** The *Nf2* knockout primary osteoblasts (OB) at differentiation stage of D7 showed decreased activity of phospho-397FAK. **b** ALP staining exhibited that over-expression of *Nf2* or *FAK* using lentivirus mediating system can sufficiently rescue the defective activities of *Nf2* mutant osteoblasts. **c** The levels of phospho-397FAK, Runx2, Sp7 and collagen type I were sufficiently rescued after the lentivirus mediated *Nf2* overexpression in *Nf2* mutant osteoblasts. **d** co-IP assay showed that FLAG-FAK and HA-NF2 forms an interaction in 293 T. **e** co-IP assay confirms that Nf2 and FAK interacted in primary osteoblasts. **f**, **g** NanoBit protein:protein interaction system (N2015, Promega) using paired Nf2 and FAK plasmids based on structural conformation (**f**) showed that C-terminal domain of Nf2 protein can physically interact with the N-terminal domain of FAK in osteoblast cell line MC3T3-E1(3T3) (**g**). **g** The bioluminescence ratios between NF2-FAK interaction and negative control ($n = 3$) were analyzed using Nano-Glo® Live-cell Reagent (N1661, Promega) (Y: bioluminescence value; X: paired plasmids, such as N represents NF2; F represents FAK; C represents C terminal; N represents N terminal; 1.1 represents LgBiT, 2.1 represents SmBiT). **h** The immunosignals of phospho-FAK (397) were largely diminished in Runx2$^+$ osteoprogenitor in *Nf2* mutants at E12.5 coronal section of the skull (arrow). **i** The immunosignals of phospho-FAK (397) were significantly reduced in *Nf2* mutants at E18.5 sagittal section of the skull. Scale bar: 20 µm in (**b**) 50 µm in (**h**, **i**). Data were expressed as means ± SD and each dot represents an individual biological replicate. *P* values were calculated by unpaired Student's t-test with two-tailed analysis without adjustments. $^*p < 0.05$. $^{**}p < 0.01$, $^{***}p < 0.001$.

FAK signaling activation sufficiently restored aberrant differentiation in *Nf2* mutant osteoblasts

To investigate the efficacy of FAK and its downstream AKT and ERK1/2 actions in osteoblasts, pharmaceutical FAK inhibitor (PF573228)[64] was used to inhibit the activity of FAK in primary osteoblasts for 12 h at D3, we found that FAK inhibition can induce decreased activities of phospho-FAK (397) at low concentration (Fig. 7a) starting from 5 µm of PF573228. The inhibitory FAK action resulted in markedly decreased activities of phospho-Erk1/2, phospho-Akt, and reduced activities of Runx2 and Sp7 in primary osteoblasts (Fig. 7a), and the concentration of FAK inhibitor displayed dose-dependent impediment to both osteoblast differentiation and activities of phospho-Erk1/2 and phospho-Akt signaling.

Next, we applied Adhesamine, a dumbbell-shaped molecule to trigger FAK actions[65] to treat primary osteoblasts for 24 h at the concentration of 20 µm, and we found that the level of phospho-FAK (397) was significantly enhanced in *Nf2* mutant osteoblasts compared to the *Nf2* mutant control and negative control (Fig. 7b). Besides, the activities of phospho-Erk1/2 and phospho-Akt and osteogenic transcriptional factor Runx2 were significantly elevated in *Nf2* mutant primary osteoblasts compared to the *Nf2* mutant control and negative control (Fig. 7b), suggesting that pharmaceutical activation of FAK on phospho-FAK(397) can sufficiently rescue the activities of downstream signaling phospho-Erk1/2 and phospho-Akt in *Nf2* mutant osteoblasts, and the flawed differentiation of osteoblasts in *Nf2* mutants can be sufficiently recovered (Fig. 7b). Furthermore, SC79 (cat # HY-18749, MCE) was a specific AKT catalyst in the cytoplasma[66]. SC79 was used to treat *Nf2* mutant osteoblasts at 20 µm. Pamoic acid disodium could (cat # HY-W010907, MCE) stimulate ERK1/2 activation[67], which was utilized to treat *Nf2* mutant osteoblasts at 50 µm. Alizarin S Red staining was used to estimate mineralization matrix in osteoblasts. We found that FAK activator can sufficiently rescue the defective calcium deposition in *Nf2* mutant osteoblasts compared to the controls for 14 days (Fig. 7c). Treating *Nf2* mutant osteoblasts for 14 days using AKT or Erk1/2 activator can sufficiently rescue the inferior ossification in *Nf2* mutant osteoblasts (Fig. 7c), suggesting that activation of PI3K/Akt or Erk1/2 signaling is sufficient to restore inferior ossification in *Nf2* mutant osteoblasts.

Nf2 deficiency in postnatal suture stem cells retarded bone regeneration of cranial defects

In order to further investigate the function of *Nf2* in mesenchymal stem cell in repairing the cranial bone defects, we generated the cranial bone defect models to drill an injury area about 2 mm^2 in the frontal and parietal bone[11,68] using inducible *Prx1-CreER*[40], which has been generally used to label suture stem cells. *Prx1*$^+$ suture stem cells reside particularly in the sutures and are accountable for osteogenic potential and bone regeneration[4,40,41]. After the injection of tamoxifen in adult mice (2 m) to induce knockout of *Nf2* in suture stem cell for five days, the cranial defects on frontal and parietal bones were generated,

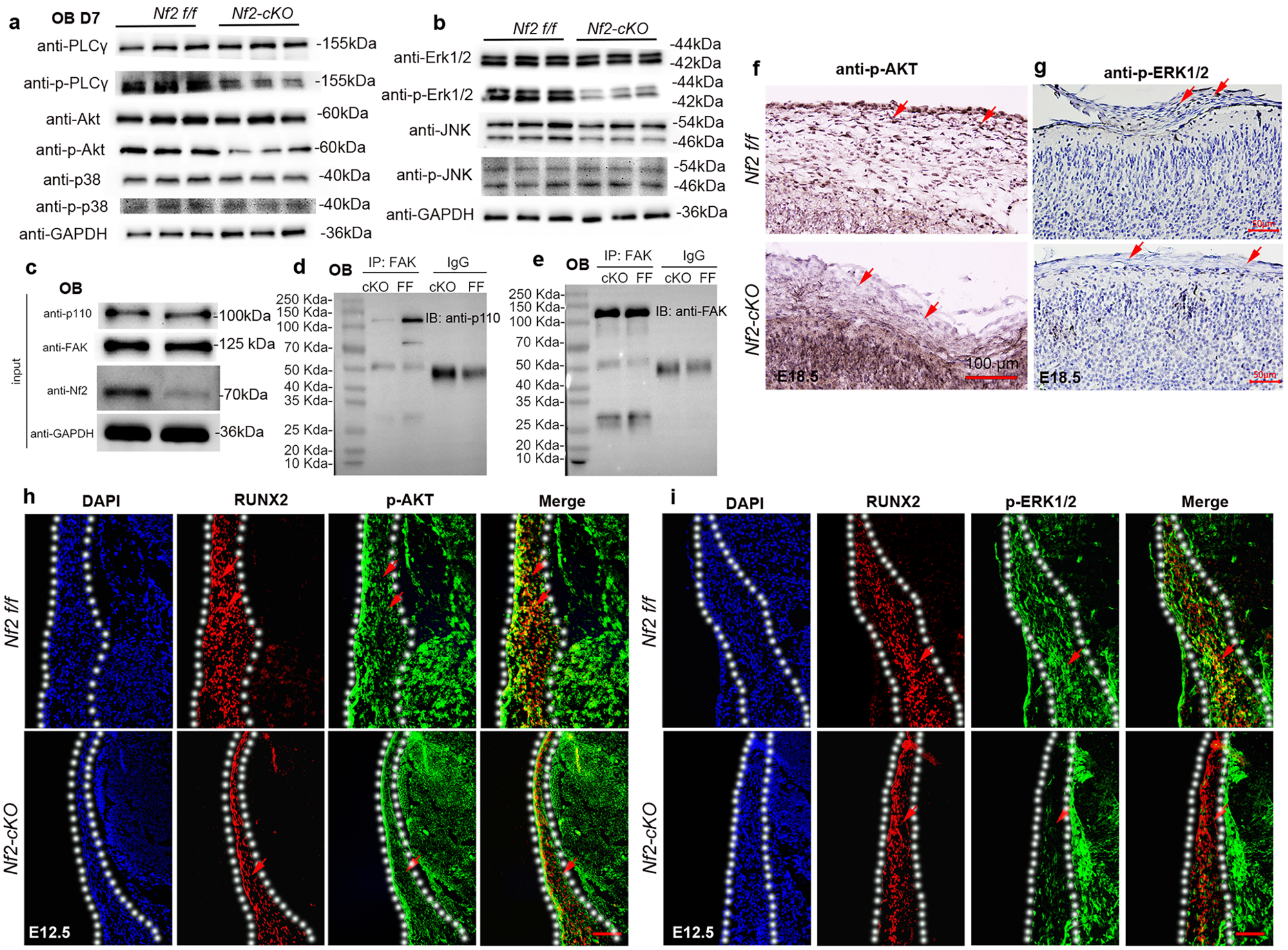

Fig. 6 | Nf2-FAK interaction mediated PI3K/AKT and ERK1/2 signaling in osteoblasts. a The activities of phospho-PLC-γ and phospho-Akt were particularly reduced in *Nf2* mutant osteoblasts. **b** The activity of phospho-Erk1/2 was specially decreased, and while the activities of phospho-p38 and phospho-JNK were not altered in *Nf2* mutant osteoblasts (**a**–**b**). **c**–**e** In *Nf2* mutant primary osteoblasts, coIP assay showed that *Nf2* deletion led to decreased connection between FAK and PI3K catalytic subunit p110. **f, g** The immunosignals of phospho-Akt and phospho-Erk1/2 at sagittal section of E18.5 skull tissue were notably reduced in *Nf2* mutants (arrow). **h, i** The immunosignals of phospho-Akt and phospho-Erk1/2 in *Nf2* mutants at the section of E12.5 cranial primordium were remarkably decreased in Runx2$^+$ osteoprogenitors (arrow). Scale bar: 50 μm in (**h**), 100 μm in (**f, i**). Data were expressed as means ± SD and each dot represents an individual biological replicate. *P* values were calculated by unpaired Student's t-test with two-tailed analysis without adjustments. OB, primary osteoblasts.

different stages post cranial bone defects (D0, D7, D14, D21, $n = 3$) were collected to visualize the healing efficacy of the damaged bones in *Nf2* mutants using *micro-CT* imaging (Fig. 8a, b). At post-injury D7, *Nf2* mutants exhibited 84.6% and 88.36% nonhealing region in frontal and parietal bones compared to the controls (frontal bone $p < 0.001$; parietal bone $p = 0.0153$). At post-injury D14, *Nf2* mutants displayed 67.2% and 70.5% nonhealing region in frontal and parietal bones, and *Nf2* controls exhibited 18.2% and 40.1% of nonhealing region in frontal and parietal bones (frontal bone $p < 0.001$; parietal $p < 0.001$). At post-injury D21, *Nf2* controls presented almost complete restoration of cranial bones defects, *Nf2* mutants displayed 17.1% and 29.5% of nonhealing area in frontal and parietal bones (frontal bone $p < 0.001$; parietal bone $p < 0.001$) (Fig. 8c), suggesting that *Nf2* deletion in suture stem cell in vivo retarded bone regeneration of cranial defects.

To trace the contribution of migrated cells at injury sites, *R26-tdTomato* was introduced to label the migrated suture stem cells/progeny. We found that *Nf2* mutants exhibited remarkably reduced migrated MSC/progeny in frontal and parietal bones compared to the control (frontal bone $p < 0.001$; parietal bone $p < 0.001$, Fig. 8d, e, $n = 3$) at post-injury D10, suggesting that the contribution of migrated MSC and its progeny to injury site was considerably defective in *Nf2* mutants. EdU$^+$/*R26-tdTomato*$^+$ cells were found distributed extensively at frontal injury sites, and still more cells could be observed at parietal injury sites (Fig. 8d, arrow), suggesting that superb capability of these EdU$^+$/*R26-tdTomato*$^+$ cells to actively proliferate and contribute to the repair and growth of the new bone. On the contrary, less EdU$^+$/*R26-tdTomato*$^+$ cells were found in *Nf2* mutant frontal and parietal injury sites, indicating an inferior osteogenic potential in *Nf2* mutant injury sites. At post-injury D7 in adult mice (2 m, $n = 3$) using skull whole-mount immunofluorescent imaging, we found that *R26-tdTomato*$^+$ suture stem cells/progeny were projecting in abundance towards (Fig. 8f, arrow) and at injury site in control mice (Fig. 8f, dotted line). In *Nf2* mutants, *R26-tdTomato*$^+$ suture stem cells/progeny were projecting less towards (Fig. 8f, arrow) and at the injury sites (Fig. 8f, dotted line) compared to the controls, suggesting that *Nf2* deficiency in *Prx1*$^+$ suture stem cells caused delayed cell migration of suture stem cells/progeny towards bone injury site (Fig. 8f, arrow). Collectively, Nf2-FAK interaction is of great importance in regulating the migration of suture stem cells/progeny and their osteogenic capacity to regenerate new bone tissues and restore the injury of cranial bones (Fig. 8g).

Discussion

In this study, we disclosed an unrecognized role of Nf2-FAK signaling axis in skeletal mesenchymal stem cells that critically required for

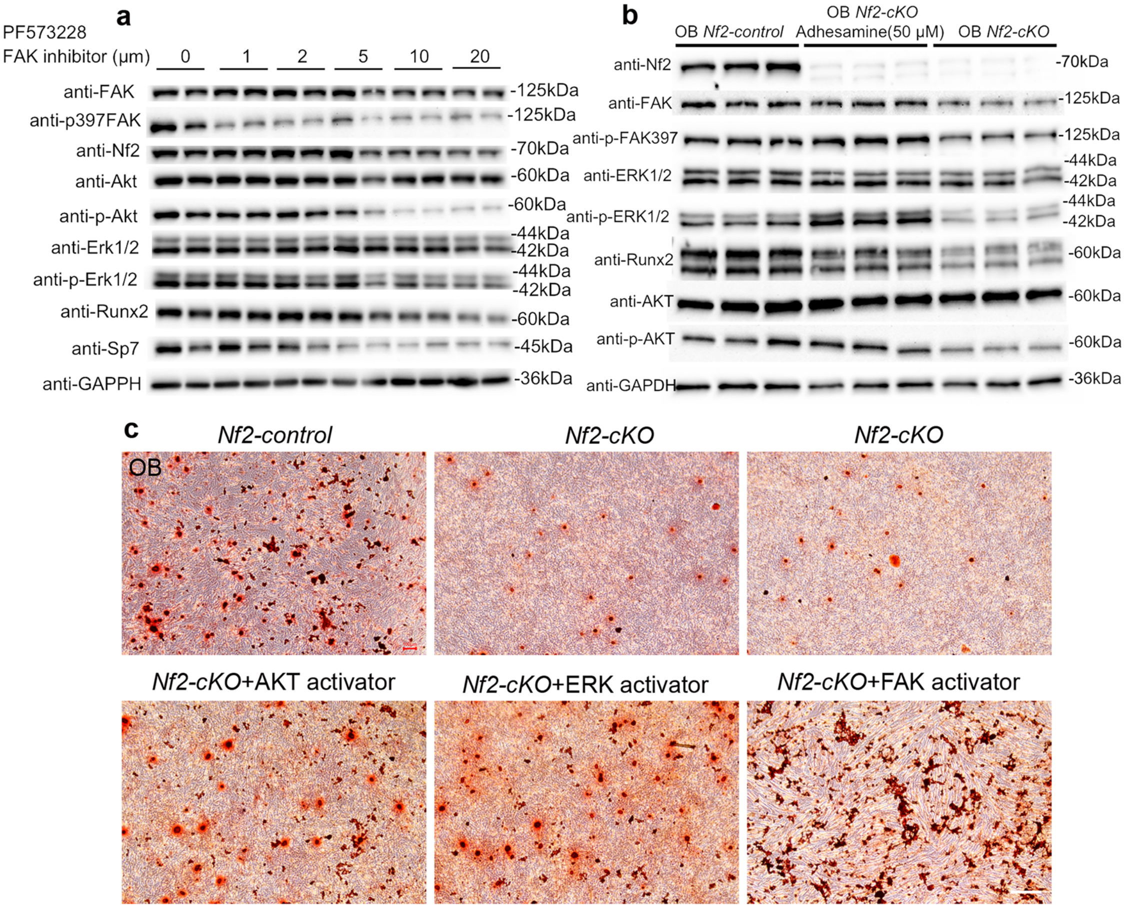

Fig. 7 | Activation of FAK mediated ERK and AKT signaling rescued the deficiency in *Nf2* mutant osteoblasts. **a** The inhibition of the FAK activity using inhibitor PF573228 resulted in significantly decreased activities of phospho-Erk1/2 and phospho-Akt and reduced activities of Runx2 and Sp7 in primary osteoblasts for 24 h. **b** The pharmaceutical activation of FAK on phospho-FAK (397) using Adhesamine (50 μM) can sufficiently rescue the activities of phospho-397FAK and its downstream signaling phospho-Erk1/2 and phospho-Akt in *Nf2* mutant osteoblasts for 24 h. **c** Adding Akt activator, Erk1/2 activator, and FAK activator in primary osteoblasts for 14 days can sufficiently rescue deficient ossification in *Nf2* mutant osteoblasts, and solvents used for the activators applied to the control groups. Data were expressed as means ± SD with at least three biological replicates. Scale bar: 50 μm in (**c**). OB, primary osteoblasts.

normalizing cranial osteoblast lineage development, cranial bones development, and bone regeneration of cranial defects. The correlations between *Nf2* expression and the sensitivity of FAK inhibitors have been established in preclinical models[69] and clinical courses[70] in tumors. *Nf2* negative tumors were susceptible to FAK inhibitors[69,71]. While in serous ovarian tumor, reduced *Nf2* expression occasionally did not cause the sensitivity to the inhibition of FAK action[72]. The reciprocal role between *Nf2* and FAK has been implied in several tumor cells[71,73,74]. However, in some *Nf2* mutant tumors, the integrins and Ras were activated, and then provoked autophosphorylation of FAK[75]. Nf2 was found directing the phosphorylation of Src and its downstream FAK[76], suggesting that the interactive role between *Nf2* and FAK was varied, directly or indirectly, in tumor cells. FAK deletion in early osteoprogenitor generated low bone mass and declined number of osteoblasts[16], flawed collagen synthesis[18], and attenuated Runx2 expression[77]. However, it remains unknown on the upstream factors governing the activity of FAK in osteoblasts. We found that *Nf2* mutants exhibited significantly decreased phospho-397FAK. *Nf2* overexpression can sufficiently rescue diminished phospho-397FAK and Runx2 in *Nf2* mutant osteoblasts, what is more, Nf2 physically interacts with FAK in osteoblasts, suggesting that *Nf2*/merlin represents an upstream governor in modulating FAK activity in osteoblasts.

FAK and its mediated downstream signaling comprised PI3K/Akt[21,22], mTOR[16] and MAPK pathways[20]. Erk1/2[58], p38 MAPK[8] and JNK pathways[59] are prominent MAPK signaling centers for osteoblast differentiation. We manifested that Nf2-FAK interaction preferentially mediated cellular Erk1/2 and Akt1/2 signaling pathways instead of JNK and p38 MAPK signaling pathways. However, in tumor cells, *Nf2* deficiency led to intense expression of ErbB2, and thus caused increasing activities of Erk1/2 and Akt/S6 in human schwannoma[78], or gave rise to the trigger of Ras-Raf-MEK-ERK1/2 signaling in tumor cells[75]. Hence, the reciprocal mechanism and the downstream signaling of FAK in tumor cells is clearly different from our discoveries that FAK mediated Erk1/2 and Akt pathway in osteoblasts. Moreover, PI3K is a heterodimer comprised of a p85 regulatory subunit and a p110 catalytic subunit[60], and engaged in osteoblasts differentiation[61,62]. In fibroblasts, FAK was found to serve as upstream of PI3K/Akt[57] and binds to PI3K-p85 regulatory subunit[63]. However, in human cancer cell lines, FAK was found negatively governed by p110[79], indicating that the action between PI3K and FAK varied in response to the types of the cells. In our study, we revealed that FAK interacts with the catalytic subunit p110-PI3K instead of p85 regulatory subunit, and *Nf2* mutant osteoblasts attenuate the association between FAK and subunit p110/PI3K, implying that Nf2-FAK positively regulates PI3K action in osteoblasts via the interaction with p110 catalytic subunit, uncovering a new scaffolding role for Nf2-FAK as upstream factor in controlling PI3K/Akt and Erk1/2 action in osteoblasts.

During the repair of cranial defects, suture stem cells will be activated, migrated, and differentiated to develop new bone and restore the injury. Modulations of BMP, FGF, Wnt, TGF signaling

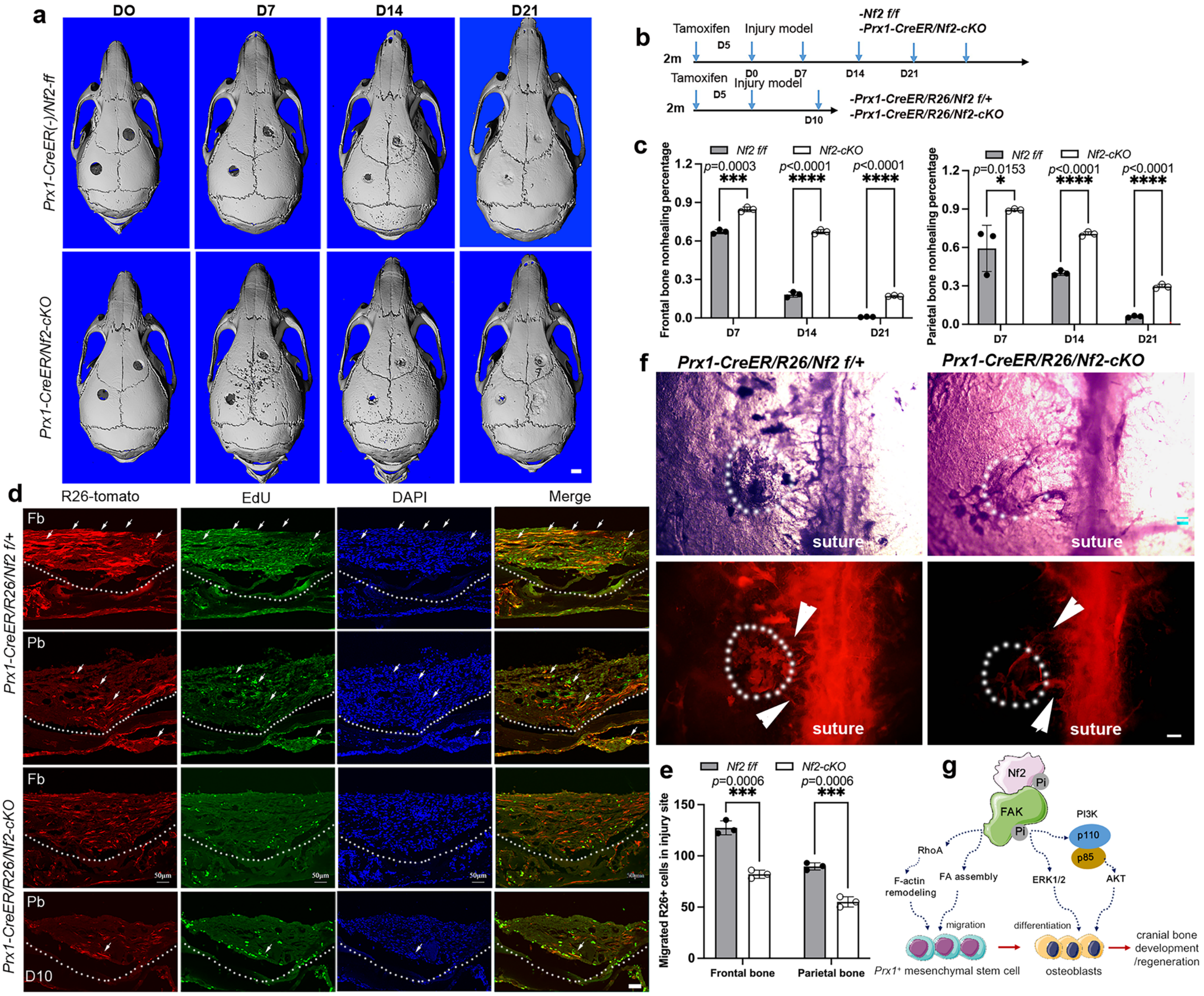

Fig. 8 | Disruption of *Nf2* in suture stem cell impaired the regeneration of cranial bone defects. **a** Cranial defects were imaged at different stage of frontal and parietal bone (D0, D7, D14, D21) in *Nf2* mutant mice (2 m, $n = 3$ at each stage) using *micro-CT*, as it indicated in the experimental design in (**b**). **c** *Nf2* mutants showed delayed healing of cranial defects at different stage of post injury (D7, D14, D21). **d** Migrated suture stem cells/progeny from the control and *Nf2* mutant mice (2 m, $n = 3$) were traced using *R26-tdTomato*, and EdU was incorporated into the mice to evaluate the proliferation of migrated cells at post-injury 10 days at injury site. *Nf2* mutant frontal and parietal bone showed less migrated suture stem cells/progeny and few EdU$^+$/*R26-tdTomato*$^+$ can be observed (**d**, **e**, arrow, $n = 3$) compared to widely distributed EdU$^+$/*R26-tdTomato*$^+$ cells at frontal and parietal injury site in the controls. **f** The whole-mount images of migrating *R26-tdTomato*$^+$ stem cells/progeny towards (arrow) and at injury sites (dotted line) at post-injury D7 upon *Nf2* deficiency in *Prx1*$^+$ suture stem cells from control and *Nf2* mutant mice (2 m, $n = 3$). **g** Mechanism of Nf2 mediated FAK signaling axis in cranial bone development and regeneration. Nf2 acts as a regulator to modulate the activity of phospho-397FAK and physically interacts with FAK. Deletion of *Nf2* leads to defective FA assembly, cytoskeletal organization to influence MSC migration. Nf2-FAK especially mediated cellular Erk1/2 and p110-PI3K/Akt signaling to regulate MSC migration and differentiation. Scale bar: 50 μm in (**a**, **d**, **f**). Data were expressed as means ± SD and each dot represents an individual biological replicate. *P* values were calculated by unpaired Student's t-test with two-tailed analysis without adjustments. $*p < 0.05$. $**p < 0.01$, $***p < 0.001$. Fb, frontal bone; Pb, parietal bone.

pathways in suture stem cells were competent in modifying osteogenic potential and the capability of cranial regeneration[4,9–11]. *Gli1*$^{+}$[80,81], *Axin2*$^{+}$[82,83], and *Prx1*$^{+}$[40] were used to label suture stem cells. *Prx1*$^+$ suture stem cells were found resident in cranial sutures[44] and postnatal periosteum[40]. Prompt migration of suture stem cells towards the injury site was essential for the repair of cranial defects. FAK was involved in gathering at the budding FAs earlier than Paxillin at cell front[27]. Variation of Paxillin-FAK connection resulted in mitigated cell adhesion[84]. Recent evidence also showed that *Nf2* functions as a component of focal adhesions in tumor cells[85,86]. We found that disturbed Nf2-FAK activity in MSC contributed to malformed focal adhesion and notably delayed MSC migration. In vivo, *R26-tdTomato*$^+$ suture stem cells/progeny were projecting much less towards and at the injury sites in *Nf2* mutant mice compared to the controls, implying delayed cell migration towards bone injury site upon *Nf2* deficiency in *Prx1*$^+$ suture stem cells.

FAK was also closely associated with bone formation[19], and acute injuries in adult skeleton can initiate FAK signaling[19], while FAK deficiency gave rise to abnormal bone matrix and delayed bone regeneration[19]. Likewise, we found that *Nf2* mutant osteoblasts exhibited diminished activities of OPN and ColI in bone matrix deposition, and impaired FAK in *Nf2* mutant mice markedly retarded bone regeneration of cranial defects. Comparably, FAK was shown critical in trafficking MSCs[87], deciding cell shape, cell motility and the physiological role of osteoblast in response to the extracellular stimuli[26], implying that *Nf2-FAK* in suture stem cells could produce considerable influences similarly on MSCs homing, motility, differentiation and physiological role of osteoblasts reacting to cranial injury. In sutures, diverse populations of suture stem cells were reported to be accountable for the cranial regeneration[11,88,89], and our finding provides a potential direction targeting classic signaling to modulate cell migration and differentiation for a better cranial bone regeneration.

In conclusion, our studies manifest that *Nf2* plays a pivotal role in normalizing osteogenic lineage development, cranial bone formation and regeneration through the modulation of FAK activity, especially pronounced in the physical Nf2-FAK interaction and its mediated cellular Erk1/2 and p110-PI3K/Akt signaling being an indispensable scaffold in the skeletal system.

Methods

Generation of *Nf2 cKO* mice

The use of animals was approved by the Institutional Animal Care and Use Committee at the Zhejiang SCI-TECH University (ethical approval number #201911001). The study was performed in compliance with the guidelines for the care and use of animals in research. All mice were on a pure C57BL/6 background and housed at 20 °C-22 °C on a 12 hr light/dark cycle with 45-55% humidity in the institutional animal facility of the Hangzhou Normal University and Zhejiang SCI-TECH University.

The *Nf2* floxed allele (*f/f*) was provided by Inserm[42]. *Prx1-Cre* was kindly provided by Prof. Bo Zhou (Shanghai Institute of Biochemistry and Cell Biology). Inducible *Prx1-Cre*^{ER} was purchased by Jacksonlab (Stock #007914). *ROSA-R26*^{tdTomato} mouse (*R26*^{tomato}) was kindly provided by Prof. Yanmei Tao (Hangzhou Normal University) to genetically label derived cells under *Prx1-Cre*^{ER} transgenic mouse line. *Nf2*$^{f/f}$ mice and mice with tissue-specific promoter-driven Cre (*Prx1-Cre* or *Prx1-Cre*^{ER}) were crossed to generate heterozygous mice, which were intercrossed to obtain homozygous cKO (conditional knockout) mice (*Prx1-Cre/Nf2*$^{f/f}$*/R26*^{tomato} *or Prx1-Cre/Nf2-cKO*). Cre-negative littermates served as controls. *Prx1-Cre/Nf2*$^{f/+}$*/R26*^{tomato} was used as a negative control to label migrated suture stem cell in cranial injury model.

Tail or toe tissue of each animal was collected for genotyping. The following primers were used for genotyping[90]: 5′-CTTCCCAGACAAGCAGGGTTC-3′ and 5′-GAA GGC AGC TTC CTT AAG TC-3′ for *Nf2*$^{f/f}$ (~442 bp) and WT (~ 305 bp) fragments; 5′-GAA GGC AGC TTC CTT AAG TC-3′ and 5′-CTC TAT TTG AGT GCG TGC CATG-3′ for the deleted allele (338 bp) driven by *Prx1-Cre* and *Prx1-Cre*^{ER}. 5′-TCC AAT TTA CTG ACC GTA CACC-3′ and 5′-CGT TTT CTT TTC GGA TCC-3′ for the Cre gene product (~372 bp). *R26*^{tomato} mutant was determined using R26Tomato-M3: 5′-GGC ATT AAA GCA GCG TAT CC-3′; R26Tomato-M5: 5′-CTG TTC CTG TAC GGC ATG-3′, and a fragment of ~196 bp can be visualized. Primers R26Tomato-WT5: 5′-AAG GGA GCT GCA GTG GAG TA-3′ and R26Tomato-WT3: 5′-CCG AAA ATC TGT GGG AAG TC-3′ were used to determine phenotype of wildtype at a fragment of ~297 bp.

Inducible knockout of Nf2 and cranial bone defects model

To induce the knockout of *Nf2* in suture mesenchymal stem cell, *Nf2*^{ff}*/Prx1-Cre*^{ER} *or Prx1-Cre/Nf2*$^{f/f}$*/R26*^{tomato} animals were treated with tamoxifen in sterile oil for 5 days (40 mg/kg, intraperitoneally), and the control were *Nf2*^{ff} or *Prx1-Cre/Nf2*$^{f/+}$*/R26*^{tomato} animals (2 m). For the cranial bone defects, it is performed based on publication[9–11]. Briefly, after mice anesthesia, disinfection was made at the surgical site of the mice, an incision was made laterally to the sagittal midline to expose the frontal and parietal bones. The pericranium was removed using a sterile cotton swab. Using diamond coated trephine bits and saline irrigation, a 2-mm^2 defect was created carefully (so as not to damage the underlying dura) in the right frontal bone and left parietal bones of the recipient mice with no damage to the underlying dura mater. Post-surgery care was made to animals to lower the pain and disinfection. EdU was injected intraperitoneally at a single dose of 100 mg/kg to each animal 2 hr before the tissues collection on day 10 and day 21.

Skeletal staining

Alizarin Red-Alcian Blue staining was used to determine the skeletal structure in embryos. Skeletons in gestation at different developmental stages were double stained for cartilage and bone using Alcian Blue and Alizarin Red solution All carcasses were skinned and fixed in 95% ethanol for 24 h. Samples were then placed in 95% ethanol-Alcian Blue (#A5268, Sigma) and Alizarin red solution (#A5533, Sigma) (24, 48 h respectively) for cartilage and bone staining, followed by a 95% ethanol wash (8 h), and maceration in 1% KOH overnight at 4 °C. Samples were cleared in 20%, 50%, 80% glycerol in 1% KOH for 12 h for each step. Samples were stored in 100% glycerol for subsequent imaging.

µ-CT analysis

Micro-computed tomography (µ-CT) was performed using Bruker Skyscan1272. For newborns, bones were scanned at 30 keV, 150 µA, and 5 µm. For adult mice, bones were scanned at 70 keV, 140 µA, and 12 µm. The scan and analysis of the trabecular bones were performed from the growth plate and consisted of 150 slices. The scan and analysis of the cortical bone were performed at the midshaft of the bone and consisted of 100 slices (12 mm per slice). Analysis was performed using the Bruker CTAn Micro-CT Software. Three-dimensional images were reconstructed using Amira-Avizo Software (Thermofisher).

Histological tissue preparation

All female and male mice were used for tissue collection. Histology and tissue preparation were performed based on our previous publications[90,91]. Briefly, pregnant mice and adult mice (2 m) were euthanized with CO_2 followed by cervical dislocation. Embryos (E12.5–E18.5) were dissected from the uterus under a microscope. E0.5 was designated as noon of the day on which the dam was positive for the vaginal plug. Murine femurs and tibiae were harvested, skinned, and eviscerated before fixing in 4% paraformaldehyde (PFA) in 1x PBS overnight. For paraffin sections, specimen was twice dehydrated in 50% and then 70% ethanol solution respectively and embedded in paraffin. Sections were cut at a thickness of 6 µm and mounted on Superfrost Plus slides (Fisher). For frozen sections, PFA-fixed tissues were cryoprotected in 30% sucrose in 0.1 M PBS at 4 °C for at least 24 hr, embedded in O.C.T. compound (Tissue Tek), and rapidly frozen for cryostat sectioning at 10 µm using Leica microtome (Leica LM 3095), and then mounted on Superfrost Plus slides (Fisher).

H&E staining

Cranial bone paraffin sections were stained with Hematoxylin buffer (BBI E607317) and Eosin buffer (BBI E607312) according to protocol, rehydrated and stained the slides in hematoxylin. Rinsed using acid alcohol (1% HCl in 50% EtOH) and counterstained with Eosin. Slides dehydrated in 100% EtOH and Xylene. Safranin O staining was performed by staining in Weigert's iron hematoxylin solution for 3 minutes, followed by Fast Green (0.001%) and Safranin O (0.1%) for 5 minutes each.

von Kossa staining

To examine mineralization, sections from E15.5 embryos were incubated in 1% silver nitrate for 30 min while under sun light. Unreacted silver was washed with 5% sodium thiosulfate and distilled water for 5 min each. The slides then incubated in 1% Alcian Blue solution for 30 min, followed counterstained with nuclear fast red solution. Sections were dehydrated and coversliped using permanent mounting medium. For cell staining and sections by von Kossa staining, firstly to wash the cells with Ca/Mg-free PBS and then fixed the slides in 4% formalin/PBS. Added silver nitrate solution and incubated the cells sequestered from any UV exposure. The unincorporated silver nitrate was removed via 5% sodium thiosulfate.

Immunostaining

For immunohistochemistry staining based on our publication[92,93], the paraffin sections were used for the experiments, sections were treated with 6% H_2O_2 in 100% methanol at room temperature for 5 h to block endogenous peroxidase activity followed by rehydration through a descending methanol series (50, 25, and 0% in 0.1 M PBS) at room temperature for 30 min each. Antigen retrieval was performed by heating the tissues at 92–95 °C for 5 min in Universal Antigen Retrieval Agent (CTS015; R&D Systems, Minneapolis, MN). PBST (0.1 M PBS and 0.1% Triton X-100) was used to block nonspecific staining. Sections were then incubated with primary antibody in 10% normal donkey serum (D9663; Sigma Aldrich, St Louis, MO) in PBST at 4 °C overnight (Supplemental Table 1). After rinses with PBS for three time, sections were incubated at 4 °C for 24 h with biotin-conjugated secondary antibody (BA-5000; Vector Laboratories, Burlingame, CA) in 1% NDS in PBST, and then incubated at room temperature for 30 min with peroxidase-conjugated streptavidin in blocking solution (PK6200; Vector Laboratories, Burlingame, CA). After three rinses in PBS, sections were preincubated in nickel-intensified DAB solution (SK4100; Vector Laboratories, Burlingame, CA) without H_2O_2 at room temperature for 30 min followed by incubation with DAB solution containing 0.0003% H_2O_2. The reaction was stopped by PBS rinses twice and photographed in 0.1 M PBS. Counterstaining by hematoxylin was dependent on sections.

For immunofluorescence (IF) staining, frozen sections were air-dried at room temperature for 1 h and rehydrated in 0.1 M PBS. Blocking of non-specific staining was carried out by incubation with 10% normal donkey serum in 0.1 M PBS containing 0.3% Triton ×-100 (×100, Sigma Aldrich, St. Louis, MO) at room temperature for 30 min. Then, the sections were incubated with primary antibodies (Supplemental Table 1) in the carrier solution (1% normal donkey serum, 0.3% Triton ×-100 in 0.1 M PBS) at 4 °C for overnight. Sections without a primary antibody treatment were used as negative control. Following three rinses in 0.1 M PBS, sections were incubated with Alexa Fluor® 488- or 647-conjugated secondary antibody (1:500, Jackson immune research, West Grove, PA) in carrier solution at room temperature for 1 h. Following rinses with 0.1 M PBS, sections were counterstained with DAPI (200 ng/ml in PBS, D1306; Life Technologies, Carlsbad, CA) at room temperature for 10 min. After thorough rinsing in 0.1 M PBS, sections were air-dried and cover slipped with Prolong®Diamond antifade mounting medium (P36970; Fisher Scientific, Waltham, MA). The sections were photographed using a laser scanning confocal microscope (Zeiss LSM 710, Zhejiang SCI-TECH University).

EdU analysis

To collect tissues for EdU immunoreactions, EdU (B5002, Beyotime, Shanghai, China) was dissolved in Dulbecco's phosphate-buffered saline (DPBS, Cytiva, Marlborough, MA) at 10 mg/ml and injected intraperitoneally at a single dose of 100 mg/kg 2 h before embryo collection. EdU staining was performed based on the BeyoClick™ EdU-594 (#C0078S, Beyotime, Shanghai, China), and EdU positive osteoprogenitor cells cells were calculated from three different samples using Imaging J.

Apoptosis assay

The apoptosis was determined using terminal deoxynucleotidyl transferase-mediated deoxyuridine triphosphate nick end-labeling (TUNEL). The frozen sections were fixed and permeabilized, followed by TUNEL labeling using a One Step TUNEL Apoptosis Assay Kit (#C1089, Beyotime, China) based on the protocol. The TUNEL positive cells were imaging using confocal microscope and counted calculated from three different samples using Imaging J.

Cell culture and differentiation assay

Primary calvarial osteoblast culture, embryonic mesenchymal stem cells (MSCs) culture, and osteogenic induction were performed as described[49,94]. Freshly sorted MSCs were seeded in 10 cm dish at a density of 500 cells/cm^2 in aMEM medium supplemented with 20% FBS and 100 IU/ml Penicillin/Streptomycin (GIBCO, Invitrogen, Carlsbad, CA, United States) based on publication[49,50,95], and the MSCs were then used for scratch assay to test the cell migration. For osteoblast culture, calvarial bones were isolated from newborn mice or embryonic stage of E18.5 from *Prx1-Cre/Nf2-cKO* mutants and *Cre$^-$/Nf2$^{f/f}$* littermates using a dissecting microscope[96,97]. After the removal of the periosteum and dura mater from the skull, the bones were then minced and digested using 0.2% dispase II and 0.1% collagenase in serum-free medium at 37 degrees. Digestion was carried out three times, and the first two digestions for 30 min were discarded, the last digestion for 90 min was pooled, centrifuged, and resuspended in aMEM supplemented with 10% FBS and 100 IU/ml Penicillin/Streptomycin (GIBCO, Invitrogen, Carlsbad, CA, United States) to reach cell confluence.

For the osteogenic differentiation assay, the confluence osteoblasts were digested using 0.25% trypin/EDTA (Thermofisher, 25200056) and the cells were seeded at in six-well plates at 2×10^5 per well. Subsequently, cells were induced using osteogenic differentiation medium and BGJb medium (12591, Gibco) supplemented with 10% (vol/vol) FBS, 50 μg/mL ascorbic acid (A4544; Sigma-Aldrich), and 5 mM glycerolphosphate (G9891; Sigma-Aldrich) and 100 IU/ml Penicillin/Streptomycin (GIBCO, Thermo, United States). Osteoblast were collected at different differentiation stage (d0, d7, d14). Osteoblastogenesis was analyzed by ALP staining at d7 according to manufacturer's manual (A2356; Sigma-Aldrich). Osteoblast mineralization was examined by Von Kossa staining at D14. RNA and proteins isolated for the analysis of osteogenic markers. During the osteogenic differentiation, activators such as Adhesamine, dumbbell-shaped molecule, activates MAPK/FAK pathway[65]. SC79 (cat # HY-18749, MCE), a unique specific AKT activator to activate AKT in the cytosol[66]. Pamoic acid disodium, which (cat # HY-W010907, MCE) induces ERK1/2 activation[67] were used to treat osteoblasts cells to evaluate the activities of osteoblast differentiation.

Cell adhesion, detach and migration assay

The cells were pretreated with precoated with fibronectin (10 μg/ml) plates. For adhesion examination, primary osteoblasts were trypsinized and diluted to a concentration of 1×10^5 cells/ml with the same medium. Then 100 μl of cells was added to each well of a 24 well plate, and the cells were incubated for different time points at 0 min, 15 min and 30 min. After discarding of the floating cells, the attached cells were fixed with 4% paraformaldehyde and stained with methylene blue; and the number of attached cells was examined by microscopy. For the detach assay, osteoblasts were grown to 90% confluency on culture plates prior to trypsinization for 2 min at 37 °C. The cells were then washed, and the remaining adherent cells were incubated for 1 h at 37 °C and the cells were counted. Two experiments were used for the migration assay, MSCs isolated from control and *Nf2-cKO* mice were used for migration assay. What is more, *Lenti-shNf2* and *Lenti-shctrl* viruses were transfected into MSC cells using the Lipo8000 transfection reagent (Beyotime, C0533) following manufacturer's instructions to reduce the effect of cell proliferation. After 24 h, scratches were made in each well using tips to create the space for cell migration, and the FBS-free aMEM medium was used for the sequent calculation of the migrated distances of the cells at different time points 0 h, 3 h, 6 h, 9 h, 12 h, 24 h. Each time points were biologically repeated at least 3 times. The migrated distances of cells were examined by microscope.

Live cell imaging

Live cell imaging was performed as described[98]. *Nf2 ff* and *Nf2-cKO* primary osteoblasts were were transiently transfected with mouse paxillin-GFP and were plated on fibronectin (10 μg/mL)-coated glass-bottom cell culture dishes before the use of a time-lapse fluorescence microscope (Olympus). Images were taken at 2.5-minute intervals and were processed for estimation of various parameters. Live cell imaging was performed in live-cell imaging buffer (Thermofisher) containing ProLong Live antifade Reagent (Thermofisher, P36974) using FV3000 Confocal laser scanning microscope (Olympus).

NanoBiT protein:protein interaction assay

NanoBiT assay was performed using Nano-Glo® Live Cell Assay System following manufacturers' instructions (N2015, Promega). Briefly, mouse *Nf2* and *FAK* cDNA sequences were cloned into pBiT1.1-C[TK/LgBiT], pBiT2.1-C[TK/SmBiT], pBiT1.1-N[TK/LgBiT] and pBiT2.1-N[TK/SmBiT] vectors by homologous recombination using the Seamless Cloning kit (Beyotime, D7010). For experimental group, 3T3 cells plated on black-wall 96-well plates were transfected with paired plasmids (pBiT-Nf2/LgBiT+pBiT-FAK/SmBit, pBiT-Nf2/SmBiT+pBiT-FAK/LgBit). For the control group, 3T3 cells on the same plate were transfected with pBiT-Nf2/LgBit or pBiT-FAK/LgBit with HaloTag-SmBiT® (negative control plasmid). Luminescence signal was detected 48 h post-transfection immediately after adding 25 µl Nano-Glo® Live-cell Reagent (N1661, Promega) using Varioskan Flash Full Wavelength Scanning Multifunction Reader (Thermofisher) at ambient temperature and 1000 ms intervals. Primers sequences are presented in Supplemental Table 2.

Lentivirus package and cell lines

Nf2 shRNA was purchased from Santa Cruz Biotechnology (sc-36053-SH, Santa Cruz, China), *Nf2* cDNA was constructed by inserting the cDNA sequence into the pLentiPGK-puro vector using Gateway Cloning (Invitrogen). For lentivirus packaging, the 2nd generation packaging plasmids (psPAX2 and pMD2.G) and lentivirus vector were co-transfected into 293 T cells using the Lipo8000 transfection reagent (Beyotime, C0533) following manufacturer's instructions as described[93], and the virus was harvested 48 and 72 h post-transfection. Viral titers were determined in 293 T cells, and lentivirus infection was performed by incubating primary cells with 5 infection units (IU) per cell (about 1×10^5 IU per well in a 24 well plate) in the presence of 10 µg/ml polybrene overnight. For the stable sh*Nf2* MC3T3-E1 (3T3) cell line screening (#1101MOU-PUMC000012, MC3T3-E1, NICR, China), puromysin (4 µg/ml, Byotime, China) was used to screen the stable transfect cells, which further maintained in puromysin (2 µg/ml, Byotime, China) in aMEM media supplemented with 10% FAS and 1% gentamysin.

Western blot assay

Proteins from cultured osteoblast at different differentiated stages from *Prx1-Cre/Nf2*^{cKO} mutants and *Cre*$^{-}$*/Nf2*$^{f/f}$ littermate controls were extracted using radioimmunoprecipitation assay (RIPA) buffer (1% NP-40, 150 mmol/L NaCl, 50 mmol/L Tris-HCI, 0.5% sodium deoxycholate, 0.1% SDS, 1 mmol/L EDTA, pH 7.4). The concentration of extracted proteins was determined using Pierce™ BCA protein assay kit (#23225, Thermo Fisher Scientific) and Synergy™ 4 microplate reader (#7161000, BioTek Instruments, Winooski, VT). An amount of total protein was loaded into each lane. Sodium dodecyl sulphate–polyacrylamide gel electrophoresis (SDS-PAGE) was used to resolve the protein bands and transferred to the nitrocellulose membrane. Non-specific binding was blocked using blocking buffer containing 3% bovine serum albumin (A-420–100, Gold Biotechnology, St Louis, MO) in Tris-buffered saline and Tween-20 buffer (TBST) buffer (20 mM Tris pH 7.5, 150 mM NaCl, 0.1% Tween 20) at room temperature for 1 h. The membranes were incubated with primary antibodies (Supplemental Table 1) in blocking buffer at 4 °C for 24 h. Following three rinses in TBST (15 min/each), membranes were incubated with conjugated secondary antibodies (#111-035-144, Jackson ImmunoResearch, West Grove, PA) in blocking buffer at room temperature for 2 h. ChemiDocMP Imaging System (Bio-Rad ChemiDoc, Hercules, CA) was used to image the Western blot bands as described[93].

co-immunoprecipitation (co-IP) assay

For co-IP, cell lysates were prepared from cells cultured on one 10 cm dish in 500 µl co-IP buffer (25 mM Tris, 150 mM NaCl, 1% NP-40, 1 mM EDTA, 5% Glycerol, pH7.4) supplemented with proteinase and phosphatase inhibitor cocktail (P1050, Beyotime, China). Cell lysates were incubated with co-IP antibody or normal IgG with rotation overnight at 4 °C. Then, Dynabeads (10001D, Thermo) were incubated for 30 min and then wash using DynaMag-2 magnet (12321D, Thermo) and eluted in SDS elution buffer (50 mM Tris, 2% SDS, 10% glycerol) at 60 °C for 10 min. The supernatant containing co-IP products was supplemented with 100 mM DTT and 0.1% Bromophenol Blue, denatured at 95 °C for 10 min, and submitted for western blot analysis.

GTPase assay

RhoA activities were evaluated using kit from Cytoskeleton (BK030, Cytoskeleton, Inc.). Briefly, the Nf2 mutant and control MSC were pretreated with fibronectin coating (10 µg/ml), when the cells reach to about 30% confluence, the cells were lysate collected, and rhotekin-RBD beads were added to lysate to pull down the RhoA based on the instruction, and Western Blotting were performed to visualize the activity of RhoA in *Nf2* mutant MSC.

Quantitative real-time reverse transcription (qRT)-PCR

Total RNA was extracted from cultured cells with TRIzol reagent (15596018, Life Technologies). Mouse cDNA was reversed-transcribed from 0.5 g total RNA with Hifair® III 1st Strand cDNA Synthesis SuperMix for qPCR (#11141ES10, YEASNE, China). The qRT-PCR was performed using one step RT-PCR System with Hieff® qPCR SYBR Green Master Mix (#11202ES03, YEASNE, China) on the ABI7500 platform. Expression levels of each gene were given relative to glyceraldehyde 3-phosphate dehydrogenase (*Gapdh*). Primers sequences are presented in Supplemental Table 3.

Statistical analysis

All data are expressed as mean ± standard deviation (SD) with at least three biological replicates. The differences between two groups were examined by two-tailed Student's unpaired t-test. One-way analysis of variance (ANOVA) was used to evaluate a statistical difference across multiple groups. A P-value less than 0.05 ($P < 0.05$) is taken as statistical significance. Prism version 9.5.1 software was used to perform statistical analysis.

Reporting summary

Further information on research design is available in the Nature Portfolio Reporting Summary linked to this article.

Data availability

The authors confirm that all relevant data are available in the paper and/or its Supplementary Information files. Source data are provided within this paper. Source data are provided with this paper.

References

1. Chen, G., Deng, C. & Li, Y. P. TGF-beta and BMP signaling in osteoblast differentiation and bone formation. *Int J. Biol. Sci.* **8**, 272–288 (2012).
2. Wu, M., Chen, G. & Li, Y. P. TGF-beta and BMP signaling in osteoblast, skeletal development, and bone formation, homeostasis and disease. *Bone Res* **4**, 16009 (2016).
3. Wu, T., Chen, G., Tian, F. & Liu, H. X. Contribution of cranial neural crest cells to mouse skull development. *Int J. Dev. Biol.* **61**, 495–503 (2017).
4. Chen, G. et al. BMP signaling in the development and regeneration of cranium bones and maintenance of calvarial stem cells. *Front Cell Dev. Biol.* **8**, 135 (2020).

5. Vanyai, H. K. et al. Control of skeletal morphogenesis by the Hippo-YAP/TAZ pathway. *Development* **147**, dev187187 (2020).
6. Liao, J. et al. Gene regulatory network from cranial neural crest cells to osteoblast differentiation and calvarial bone development. *Cell Mol. Life Sci.* **79**, 158 (2022).
7. Greenblatt, M. B. et al. The p38 MAPK pathway is essential for skeletogenesis and bone homeostasis in mice. *J. Clin. Invest* **120**, 2457–2473 (2010).
8. Wang, Y. et al. p38 Inhibition ameliorates skin and skull abnormalities in Fgfr2 Beare-Stevenson mice. *J. Clin. Invest* **122**, 2153–2164 (2012).
9. Quarto, N. et al. Origin matters: differences in embryonic tissue origin and Wnt signaling determine the osteogenic potential and healing capacity of frontal and parietal calvarial bones. *J. Bone Min. Res* **25**, 1680–1694 (2010).
10. Senarath-Yapa, K. et al. Small molecule inhibition of transforming growth factor beta signaling enables the endogenous regenerative potential of the mammalian calvarium. *Tissue Eng. Part A* **22**, 707–720 (2016).
11. Maruyama, T. et al. BMPR1A maintains skeletal stem cell properties in craniofacial development and craniosynostosis. *Sci. Transl. Med.* **13**, eabb4416 (2021).
12. Yu, M. et al. Cranial suture regeneration mitigates skull and neurocognitive defects in craniosynostosis. *Cell* **184**, 243–256 (2021).
13. Salasznyk, R. M., Klees, R. F., Boskey, A. & Plopper, G. E. Activation of FAK is necessary for the osteogenic differentiation of human mesenchymal stem cells on laminin-5. *J. Cell Biochem* **100**, 499–514 (2007).
14. Hu, P. et al. Fak silencing impairs osteogenic differentiation of bone mesenchymal stem cells induced by uniaxial mechanical stretch. *J. Dent. Sci.* **14**, 225–233 (2019).
15. Huang, Y., Liao, J., Vlashi, R. & Chen, G. Focal adhesion kinase (FAK): Its structure, characteristics, and signaling in skeletal system. *Cell Signal,* **111**, 110852 (2023).
16. Qi, S. et al. FAK promotes early osteoprogenitor cell proliferation by enhancing mTORC1 signaling. *J. Bone Min. Res* **35**, 1798–1811 (2020).
17. Sun, C. et al. FAK promotes osteoblast progenitor cell proliferation and differentiation by enhancing Wnt signaling. *J. Bone Min. Res* **31**, 2227–2238 (2016).
18. Rajshankar, D., Wang, Y. & McCulloch, C. A. Osteogenesis requires FAK-dependent collagen synthesis by fibroblasts and osteoblasts. *FASEB J.* **31**, 937–953 (2017).
19. Kim, J. B. et al. Reconciling the roles of FAK in osteoblast differentiation, osteoclast remodeling, and bone regeneration. *Bone* **41**, 39–51 (2007).
20. Zheng, W., Gu, X., Sun, X., Wu, Q. & Dan, H. FAK mediates BMP9-induced osteogenic differentiation via Wnt and MAPK signaling pathway in synovial mesenchymal stem cells. *Artif. Cells Nanomed. Biotechnol.* **47**, 2641–2649 (2019).
21. Dong, W. et al. PTX3 promotes osteogenic differentiation by triggering HA/CD44/FAK/AKT positive feedback loop in an inflammatory environment. *Bone* **154**, 116231 (2022).
22. Gunn, S. A. et al. Focal adhesion kinase inhibitors prevent osteoblast mineralization in part due to suppression of Akt-mediated stabilization of osterix. *J. Bone Oncol.* **34**, 100432 (2022).
23. Brown, M. C., Cary, L. A., Jamieson, J. S., Cooper, J. A. & Turner, C. E. Src and FAK kinases cooperate to phosphorylate paxillin kinase linker, stimulate its focal adhesion localization, and regulate cell spreading and protrusiveness. *Mol. Biol. Cell* **16**, 4316–4328 (2005).
24. Bachmann, M., Skripka, A., Weissenbruch, K., Wehrle-Haller, B. & Bastmeyer, M. Phosphorylated paxillin and phosphorylated FAK constitute subregions within focal adhesions. *J. Cell Sci.* **135**, jcs258764 (2022).
25. Webb, D. J. et al. FAK-Src signalling through paxillin, ERK and MLCK regulates adhesion disassembly. *Nat. Cell Biol.* **6**, 154–161 (2004).
26. Takahashi, M. O. et al. Growth hormone stimulates tyrosine phosphorylation of focal adhesion kinase (p125(FAK)) and actin stress fiber formation in human osteoblast-like cells, Saos2. *Biochem Biophys. Res Commun.* **263**, 100–106 (1999).
27. Hu, Y. L. et al. FAK and paxillin dynamics at focal adhesions in the protrusions of migrating cells. *Sci. Rep.* **4**, 6024 (2014).
28. Evans, D. G. et al. A clinical study of type 2 neurofibromatosis. *Q J. Med* **84**, 603–618 (1992).
29. Gutmann, D. H. et al. The diagnostic evaluation and multidisciplinary management of neurofibromatosis 1 and neurofibromatosis 2. *JAMA* **278**, 51–57 (1997).
30. Vlashi, R. et al. The molecular biology of NF2/Merlin on tumorigenesis and development. *FASEB J.* **38**, e23809 (2024).
31. Haase, V. H., Trofatter, J. A., MacCollin, M., Gusella, TarttelinE. & Ramesh, J. F. V. The murine NF2 homologue encodes a highly conserved merlin protein with alternative forms. *Hum. Mol. Genet* **3**, 407–411 (1994).
32. Bretscher, A., Chambers, D., Nguyen, R. & Reczek, D. ERM-Merlin and EBP50 protein families in plasma membrane organization and function. *Annu Rev. Cell Dev. Biol.* **16**, 113–143 (2000).
33. Bretscher, A., Edwards, K. & Fehon, R. G. ERM proteins and merlin: integrators at the cell cortex. *Nat. Rev. Mol. Cell Biol.* **3**, 586–599 (2002).
34. Akhmametyeva, E. M. et al. Regulation of the neurofibromatosis 2 gene promoter expression during embryonic development. *Dev. Dyn.* **235**, 2771–2785 (2006).
35. Hu, B. et al. Physiological signatures of dual embryonic origins in mouse skull vault. *Cell Physiol. Biochem* **43**, 2525–2534 (2017).
36. McClatchey, A. I., Saotome, I., Ramesh, V., Gusella, J. F. & Jacks, T. The Nf2 tumor suppressor gene product is essential for extraembryonic development immediately prior to gastrulation. *Genes Dev.* **11**, 1253–1265 (1997).
37. Larsson, J. et al. Nf2/merlin regulates hematopoietic stem cell behavior by altering microenvironmental architecture. *Cell Stem Cell* **3**, 221–227 (2008).
38. Liu, H. et al. Prrx1 marks stem cells for bone, white adipose tissue and dermis in adult mice. *Nat. Genet* **54**, 1946–1958 (2022).
39. Solidum, J. G. N., Jeong, Y., Heralde, F. 3rd. & Park, D. Differential regulation of skeletal stem/progenitor cells in distinct skeletal compartments. *Front Physiol.* **14**, 1137063 (2023).
40. Wilk, K. et al. Postnatal calvarial skeletal stem cells expressing PRX1 reside exclusively in the calvarial sutures and are required for bone regeneration. *Stem Cell Rep.* **8**, 933–946 (2017).
41. Takarada, T. et al. Genetic analysis of Runx2 function during intramembranous ossification. *Development* **143**, 211–218 (2016).
42. Giovannini, M. et al. Conditional biallelic Nf2 mutation in the mouse promotes manifestations of human neurofibromatosis type 2. *Genes Dev.* **14**, 1617–1630 (2000).
43. Logan, M. et al. Expression of Cre Recombinase in the developing mouse limb bud driven by a Prxl enhancer. *Genesis* **33**, 77–80 (2002).
44. Seo, H. S. & Serra, R. Tgfbr2 is required for development of the skull vault. *Dev. Biol.* **334**, 481–490 (2009).
45. Ho, T. V. et al. Integration of comprehensive 3D microCT and signaling analysis reveals differential regulatory mechanisms of craniofacial bone development. *Dev. Biol.* **400**, 180–190 (2015).
46. Robledo, R. F., Rajan, L., Li, X. & Lufkin, T. The Dlx5 and Dlx6 homeobox genes are essential for craniofacial, axial, and appendicular skeletal development. *Genes Dev.* **16**, 1089–1101 (2002).
47. Han, J. et al. Concerted action of Msx1 and Msx2 in regulating cranial neural crest cell differentiation during frontal bone development. *Mech. Dev.* **124**, 729–745 (2007).

48. Ishii, M. et al. Msx2 and Twist cooperatively control the development of the neural crest-derived skeletogenic mesenchyme of the murine skull vault. *Development* **130**, 6131–6142 (2003).
49. Bartoletti, G., Dong, C., Umar, M. & He, F. Pdgfra regulates multipotent cell differentiation towards chondrocytes via inhibiting Wnt9a/beta-catenin pathway during chondrocranial cartilage development. *Dev. Biol.* **466**, 36–46 (2020).
50. Maruyama, T., Yu, H. I. & Hsu, W. Skeletal stem cell isolation from cranial suture mesenchyme and maintenance of stemness in culture. *Bio Protoc.* **12**, e4339 (2022).
51. Subauste, M. C. et al. Vinculin modulation of paxillin-FAK interactions regulates ERK to control survival and motility. *J. Cell Biol.* **165**, 371–381 (2004).
52. Turner, C. E. Paxillin and focal adhesion signalling. *Nat. Cell Biol.* **2**, E231–E236 (2000).
53. Kawada, I. et al. Paxillin mutations affect focal adhesions and lead to altered mitochondrial dynamics: relevance to lung cancer. *Cancer Biol. Ther.* **14**, 679–691 (2013).
54. Raj, G. V., et al. Estrogen receptor coregulator binding modulators (ERXs) effectively target estrogen receptor positive human breast cancers. *Elife* **6**, e26857 (2017).
55. Bodle, C. R., Hayes, M. P., O'Brien, J. B. & Roman, D. L. Development of a bimolecular luminescence complementation assay for RGS: G protein interactions in cells. *Anal. Biochem* **522**, 10–17 (2017).
56. Zhang, X. et al. Focal adhesion kinase promotes phospholipase C-gamma1 activity. *Proc. Natl Acad. Sci. USA* **96**, 9021–9026 (1999).
57. Xia, H., Nho, R. S., Kahm, J., Kleidon, J. & Henke, C. A. Focal adhesion kinase is upstream of phosphatidylinositol 3-kinase/Akt in regulating fibroblast survival in response to contraction of type I collagen matrices via a beta 1 integrin viability signaling pathway. *J. Biol. Chem.* **279**, 33024–33034 (2004).
58. De Simone, A. et al. Control of osteoblast regeneration by a train of Erk activity waves. *Nature* **590**, 129–133 (2021).
59. Matsuguchi, T. et al. JNK activity is essential for Atf4 expression and late-stage osteoblast differentiation. *J. Bone Min. Res* **24**, 398–410 (2009).
60. Jimenez, C., Hernandez, C., Pimentel, B. & Carrera, A. C. The p85 regulatory subunit controls sequential activation of phosphoinositide 3-kinase by Tyr kinases and Ras. *J. Biol. Chem.* **277**, 41556–41562 (2002).
61. Fujita, T. et al. Runx2 induces osteoblast and chondrocyte differentiation and enhances their migration by coupling with PI3K-Akt signaling. *J. Cell Biol.* **166**, 85–95 (2004).
62. Guntur, A. R. & Rosen, C. J. The skeleton: a multi-functional complex organ: new insights into osteoblasts and their role in bone formation: the central role of PI3Kinase. *J. Endocrinol.* **211**, 123–130 (2011).
63. Hong, M. et al. Non-Smad transforming growth factor-beta signaling regulated by focal adhesion kinase binding the p85 subunit of phosphatidylinositol 3-kinase. *J. Biol. Chem.* **286**, 17841–17850 (2011).
64. Beerli, C. et al. Vaccinia virus hijacks EGFR signalling to enhance virus spread through rapid and directed infected cell motility. *Nat. Microbiol* **4**, 216–225 (2019).
65. Hoshino, M., Tsujimoto, T., Yamazoe, S., Uesugi, M. & Terada, S. Adhesamine, a new synthetic molecule, accelerates differentiation and prolongs survival of primary cultured mouse hippocampal neurons. *Biochem J.* **427**, 297–304 (2010).
66. Jo, H. et al. Small molecule-induced cytosolic activation of protein kinase Akt rescues ischemia-elicited neuronal death. *Proc. Natl Acad. Sci. USA* **109**, 10581–10586 (2012).
67. Zhao, P. et al. Targeting of the orphan receptor GPR35 by pamoic acid: a potent activator of extracellular signal-regulated kinase and beta-arrestin2 with antinociceptive activity. *Mol. Pharm.* **78**, 560–568 (2010).
68. Menon, S. et al. Skeletal stem and progenitor cells maintain cranial suture patency and prevent craniosynostosis. *Nat. Commun.* **12**, 4640 (2021).
69. Shapiro, I. M. et al. Merlin deficiency predicts FAK inhibitor sensitivity: a synthetic lethal relationship. *Sci. Transl. Med* **6**, 237ra268 (2014).
70. Soria, J. C. et al. A phase I, pharmacokinetic and pharmacodynamic study of GSK2256098, a focal adhesion kinase inhibitor, in patients with advanced solid tumors. *Ann. Oncol.* **27**, 2268–2274 (2016).
71. Poulikakos, P. I. et al. Re-expression of the tumor suppressor NF2/merlin inhibits invasiveness in mesothelioma cells and negatively regulates FAK. *Oncogene* **25**, 5960–5968 (2006).
72. Shah, N. R. et al. Analyses of merlin/NF2 connection to FAK inhibitor responsiveness in serous ovarian cancer. *Gynecol. Oncol.* **134**, 104–111 (2014).
73. Torres-Ayuso, P. et al. TNIK is a therapeutic target in lung squamous cell carcinoma and regulates FAK activation through Merlin. *Cancer Discov.* **11**, 1411–1423 (2021).
74. Ou, W. B. et al. Co-targeting of FAK and MDM2 triggers additive antiproliferative effects in mesothelioma via a coordinated reactivation of p53. *Br. J. Cancer* **115**, 1253–1263 (2016).
75. Ammoun, S. & Hanemann, C. O. Emerging therapeutic targets in schwannomas and other merlin-deficient tumors. *Nat. Rev. Neurol.* **7**, 392–399 (2011).
76. Houshmandi, S. S., Emnett, R. J., Giovannini, M. & Gutmann, D. H. The neurofibromatosis 2 protein, merlin, regulates glial cell growth in an ErbB2- and Src-dependent manner. *Mol. Cell Biol.* **29**, 1472–1486 (2009).
77. Schneider, G. B., Zaharias, R., Seabold, D. & Stanford, C. Integrin-associated tyrosine kinase FAK affects Cbfa1 expression. *J. Orthop. Res* **29**, 1443–1447 (2011).
78. Stonecypher, M. S., Chaudhury, A. R., Byer, S. J. & Carroll, S. L. Neuregulin growth factors and their ErbB receptors form a potential signaling network for schwannoma tumorigenesis. *J. Neuropathol. Exp. Neurol.* **65**, 162–175 (2006).
79. Tzenaki, N., Aivaliotis, M. & Papakonstanti, E. A. Focal adhesion kinase phosphorylates the phosphatase and tensin homolog deleted on chromosome 10 under the control of p110delta phosphoinositide-3 kinase. *FASEB J.* **29**, 4840–4852 (2015).
80. Park, S., Zhao, H., Urata, M. & Chai, Y. Sutures possess strong regenerative capacity for calvarial bone injury. *Stem Cells Dev.* **25**, 1801–1807 (2016).
81. Zhao, H. et al. The suture provides a niche for mesenchymal stem cells of craniofacial bones. *Nat. Cell Biol.* **17**, 386–396 (2015).
82. Maruyama, T. Stem cells of the suture mesenchyme in craniofacial bone development, repair and regeneration. *Keio J. Med* **68**, 42 (2019).
83. Maruyama, T., Jeong, J., Sheu, T. J. & Hsu, W. Stem cells of the suture mesenchyme in craniofacial bone development, repair and regeneration. *Nat. Commun.* **7**, 10526 (2016).
84. Deramaudt, T. B. et al. Altering FAK-paxillin interactions reduces adhesion, migration and invasion processes. *PLoS One* **9**, e92059 (2014).
85. Lallemand, D., Curto, M., Saotome, I., Giovannini, M. & McClatchey, A. I. NF2 deficiency promotes tumorigenesis and metastasis by destabilizing adherens junctions. *Genes Dev.* **17**, 1090–1100 (2003).
86. Hennigan, R. F., Fletcher, J. S., Guard, S. & Ratner, N. Proximity biotinylation identifies a set of conformation-specific interactions between Merlin and cell junction proteins. *Sci. Signal* **12**, eaau8749 (2019).
87. Zhang, Y., Ma, C., Yu, Y., Liu, M. & Yi, C. Are CXCL13/CXCR5/FAK critical regulators of MSCs migration and differentiation? *Med Hypotheses* **84**, 213–215 (2015).
88. Guo, Y. et al. BMP-IHH-mediated interplay between mesenchymal stem cells and osteoclasts supports calvarial bone homeostasis and repair. *Bone Res* **6**, 30 (2018).

89. Doro, D. H., Grigoriadis, A. E. & Liu, K. J. Calvarial suture-derived stem cells and their contribution to cranial bone repair. *Front Physiol.* **8**, 956 (2017).
90. Ishan, M. et al. Deletion of Nf2 in neural crest-derived tongue mesenchyme alters tongue shape and size, Hippo signalling and cell proliferation in a region- and stage-specific manner. *Cell Prolif.* **54**, e13144 (2021).
91. Ishan, M. et al. Increased activity of mesenchymal ALK2-BMP signaling causes posteriorly truncated microglossia and disorganization of lingual tissues. *Genesis* **58**, e23337 (2020).
92. Chen, G. et al. Specific and spatial labeling of P0-Cre versus Wnt1-Cre in cranial neural crest in early mouse embryos. *Genesis* **55**, https://doi.org/10.1002/dvg.23034 (2017).
93. Hu, S. et al. Ap-2beta regulates cranial osteogenic potential via the activation of Wnt/beta-catenin signaling pathway. *Dev. Biol.* **501**, 81–91 (2023).
94. Soleimani, M. & Nadri, S. A protocol for isolation and culture of mesenchymal stem cells from mouse bone marrow. *Nat. Protoc.* **4**, 102–106 (2009).
95. Kong, L. et al. Isolation and characterization of human suture mesenchymal stem cells in vitro. *Int J. Stem Cells* **13**, 377–385 (2020).
96. Wu, M. et al. Cbfbeta governs osteoblast-adipocyte lineage commitment through enhancing beta-catenin signaling and suppressing adipogenesis gene expression. *Proc. Natl Acad. Sci. USA* **114**, 10119–10124 (2017).
97. Wu, M. et al. Deletion of core-binding factor beta (Cbfbeta) in mesenchymal progenitor cells provides new insights into Cbfbeta/Runxs complex function in cartilage and bone development. *Bone* **65**, 49–59 (2014).
98. Iwayama, T. et al. Osteoblastic lysosome plays a central role in mineralization. *Sci. Adv.* **5**, eaax0672 (2019).

Acknowledgements

This work was supported by grants by Zhejiang Provincial Natural Science Foundation of China (LZ23H140001 to GQ CHEN), funds from National Natural Science Foundation of China (81400489, to GQ CHEN, 81900806 to CHZHOU, 32070814 to MR WU), Zhejiang Qianjiang Talent Program (21040040-E, to GQ CHEN), a startup grant from Zhejiang Sci-Tech University (18042290-Y, to GQ CHEN), the Fundamental Research Funds of Zhejiang Sci-Tech University (2021Q031), Jiaxing Science Technology Foundation (2023AY11045 & 2020AY10001, to XG ZHANG). We thank Professor Zefu Lu (Chinese Academy of Agricultural Sciences) and Ms. Rexhina Vlashi for their critical review and discussions with the manuscript. We apologize to many researchers whose work could not be cited due to space limitations.

Author contributions

Conceptualization: G.C., M.W., X.Z. Methodology: J.L., Y.H., F.S., C.Z., Y.Y., X.Z., C.Z. Investigation: J.L., Y.H., F.S., C.Z., Y.Y., X.Z., C.Z. Visualization: J.L., Y.H., F.S., C.Z., X.Z., C.Z., M.Wu., G.C. Writing—original draft: J.L., G.C. Writing—review & editing: G.C., M.Wu., J.L., Y.H. Supervision: G.C., M.Wu., X.Z. All the authors reviewed and approved the paper.

Competing interests

The authors declare no competing interests.

Additional information

Supplementary information The online version contains supplementary material available at https://doi.org/10.1038/s41467-025-57808-4.

Correspondence and requests for materials should be addressed to Xingen Zhang, Mengrui Wu or Guiqian Chen.

Peer review information *Nature Communications* thanks the anonymous reviewers for their contribution to the peer review of this work. A peer review file is available.